Acta Pharmaceutica Sinica B 2026;16(6):3698−3728

Chinese Pharmaceutical Association
Institute of Materia Medica, Chinese Academy of Medical Sciences

Acta Pharmaceutica Sinica B

www.elsevier.com/locate/apsb
www.sciencedirect.com

ORIGINAL ARTICLE

(+)-Miliusol suppresses the Warburg effect and induces regulated cell death in triple-negative breast cancer through targeting EIF3D and remodeling cancer metabolism

Jin Zhang[a,†], Lin Jia[b,†], Xiya Chen[a,b,†], Yan Wu[a], Xiaohan Sun[b], Ling Zou[d], Xiaoling Cheng[a,b], Jingnan Huang[c], Hongchao Zhou[c], Lingyun Dai[c], Le Zhou[b], Zhendan He[b], Bo Liu[d,e,*], Yue Hao[a,*], Dahong Yao[b,*]

[a]*School of Pharmacy, Shenzhen University Medical School, Shenzhen University, Shenzhen 518060, China*
[b]*College of Pharmacy, Shenzhen Technology University, Shenzhen 518118, China*
[c]*Department of Geriatrics, and Shenzhen Clinical Research Centre for Geriatrics, Shenzhen People's Hospital, School of Medicine, Southern University of Science and Technology, Shenzhen 518020, China*
[d]*Department of Biotherapy, Cancer Center and State Key Laboratory of Biotherapy, West China Hospital, Sichuan University, Chengdu 610041, China*
[e]*Institute of Precision Drug Innovation and Cancer Center, the Second Hospital of Dalian Medical University, Dalian 116023, China*

Received 24 June 2025; received in revised form 11 September 2025; accepted 11 November 2025

KEY WORDS

TNBC;
(+)-Miliusol;
Warburg effect;
Metabolic reprogramming;
EIF3D;
Autophagy;

Abstract Triple-negative breast cancer (TNBC) exhibits marked molecular heterogeneity, posing ongoing therapeutic challenges. Metabolic reprogramming, particularly through the Warburg effect, offers a promising therapeutic target for TNBC treatment. Data mining and machine learning identified (+)-miliusol as a promising candidate. Its direct target, eukaryotic initiation factor 3D (EIF3D), was validated through mass spectrometry-coupled cellular thermal shift assay (MS-CETSA), a biotinylated probe, and a proteolysis-targeting chimera (PROTAC) approach. EIF3D, an emerging oncoprotein and atypical translation initiation regulator, promotes tumor survival by selectively modulating protein synthesis. (+)-Miliusol demonstrates potent anti-proliferative and anti-migratory activity against TNBC in both

*Corresponding authors.
E-mail addresses: liubo2400@163.com (Bo Liu), yuehao@szu.edu.cn (Yue Hao), yaodahong@sztu.edu.cn (Dahong Yao).
†These authors made equal contributions to this work.

Peer review under the responsibility of Chinese Pharmaceutical Association and Institute of Materia Medica, Chinese Academy of Medical Sciences.

https://doi.org/10.1016/j.apsb.2026.03.021

ER stress

in vitro and *in vivo*. Integrated proteomic and transcriptomic analyses revealed that (+)-miliusol suppresses TNBC progression through EIF3D-mediated translational regulation. Mechanistically, it disrupts the EIF3D−AlkB homolog 5 (ALKBH5)−glucose transporter type 4 (GLUT4) axis, EIF3D−HIF1α signaling, and the EIF3D−RuvB like AAA ATPase 1 (RUVBL1)−β-catenin pathway, thereby inhibiting glycolysis and metastasis while inducing ER stress-dependent apoptosis *via* caspase-12 and JNK activation. Additionally, (+)-miliusol blocks EIF3D−HIF1α and EIF3D−ALKBH3 interactions, impairing ATAD2/PAK1-regulated Warburg-effect networks and triggering autophagy-associated cell death. (+)-Miliusol induces TNBC cell death by selectively suppressing translation of critical glycolytic and metastatic regulators. These findings establish EIF3D-mediated translational control as a promising therapeutic avenue for TNBC treatment.

1. Introduction

Breast cancer is the most prevalent type of human malignancies in women. It was reported that breast cancer has surpassed lung cancer in terms of incidence for the first time in 2020, establishing itself as the leading malignancy worldwide[1]. Among the subtypes of breast cancer, TNBC, which is defined by the absence of estrogen receptor (ER), progesterone receptor (PR), and human epidermal growth factor receptor 2 (HER2) amplification, is one of the most prominent subtypes, accounting for approximately 15%−20% of all breast cancer cases[2]. TNBC poses significant challenges to therapeutic interventions due to its marked heterogeneity and the absence of effective therapeutic targets. This, in turn, results in a high recurrence rate, augmented metastatic potential, and diminished overall survival rates[3]. Despite advances in targeted drug therapies (such as poly ADP-ribose polymerase (PARP) inhibitors and protein kinase B (AKT) inhibitors)[4,5], immunotherapy (such as camrelizumab)[6], and gene therapy[7], their applications in TNBC are still limited, and the outlook remains uncertain. Therefore, there is an urgent need to identify and develop innovative therapeutic alternatives for TNBC. Although currently personalized therapy appears to be an optimal choice for TNBC treatment, achieving individualized treatment medications and regimens for each patient remains a challenge. Accordingly, accurate identification of intrinsic commonalities of TNBC and precise classification from its high heterogeneity may offer greater potential for its therapeutics.

TNBC classification currently relies on gene/protein expression profiles and immunohistochemical biomarker panels. However, therapeutic outcomes predicted by conventional subtyping methods remain suboptimal due to TNBC's dynamic mutational landscape. Notably, metabolic reprogramming represents a fundamental hallmark of cancer cells. Consequently, targeting tumor metabolism emerges as both a conceptually innovative and therapeutically viable strategy for TNBC treatment. It has been observed that more than one-third of TNBC cases exhibit a preference for glycolysis as their metabolic mode[8]. Interestingly, aerobic glycolysis (known as the Warburg effect) stands for the most well-known and studied manner of tumor metabolic reprogramming. Warburg effect states that even with sufficient oxygen, cells will still choose glycolysis, a less productive manner for energy, rather than the more efficient OXPHOS[9]. The Warburg effect enhances cellular energy production efficiency, while lactate accumulation promotes tumor microenvironment acidification, thereby exacerbating genomic instability and malignant progression. Consequently, the utilisation of glycolytic inhibition as a therapeutic modality for TNBC has proven to be a promising approach, exhibiting the potential for tangible clinical benefits[8]. Recently, regulating mitochondrial metabolism and immune microenvironment has shown promising prospects in the treatment of TNBC[10,11].

The translation of mRNA in cancer cells exhibits a profound alteration as compared to that in normal ones. The tumor will inhibit or activate the translation of specific mRNAs in response to various pressures on tumor survival. EIF3D, a component of the EIF3 complex, primarily participates in controlling the translation of mRNA[12]. Accumulating evidence has shown that EIF3D plays a significant role in the advancement and growth of cancer by modulating the translation of specific proteins. For instance, knock out of *EIF3D* significantly reduced the expression of multiple marker proteins for the epithelial−mesenchymal transition (EMT) (such as Vimentin, N-cadherin, MMP1, etc.) in breast cancer cells, indicating its important role in cell metastasis[13]. In addition, the activation of the phosphoinositide 3-kinase (PI3K)−AKT signaling pathway by EIF3D may contribute to the progression of gallbladder cancer[14]. Notably, EIF3D has been reported to promote the Warburg effect in cervical cancer cells by inhibiting the degradation of GRP78, suggesting that it might be of great potential to suppress the Warburg effect of cancer cells by targeting EIF3D[15].

Natural product-derived small molecules exhibiting potent anti-tumor properties represent a valuable source for drug discovery, particularly as lead compounds targeting cancer-associated metabolic reprogramming—a hallmark of malignant progression. Among them, (+)-miliusol is an active natural product, which was first isolated from *Miliusa balansae* Fin. & Gagn. in 2004[16]. (+)-Miliusol has been shown with broad-spectrum anti-tumor activity, including colon cancer, melanoma, lung cancer, and cervical cancer[17]. However, the mechanistic effects of (+)-miliusol in breast cancer, particularly in the context of TNBC, remain poorly understood. Crucially, the molecular targets and associated regulatory networks underlying its anti-tumor activity have yet to be systematically characterized.

Through systematic data mining and high-throughput screening of natural product libraries, we identified (+)-miliusol as a novel glycolysis inhibitor targeting the Warburg effect. This compound has been shown to effectively suppress the glycolysis, proliferation and metastasis of TNBC cells in both *in vitro* and *in vivo* models. Multi-omics profiling revealed EIF3D as the direct molecular target, through which (+)-miliusol coordinately

disrupts: (1) the EIF3D−ALKBH5−GLUT4 axis regulating glucose metabolism, and (2) the EIF3D−RUVBL1−β-catenin signaling cascade. Mechanistically, (+)-miliusol triggers an integrated cell death network involving concurrent autophagy induction, endoplasmic reticulum stress (ER stress) activation, and apoptotic signaling. Furthermore, transcriptional repression of *PAK1* encodes p21-activated kinase1 (PAK1) and ATPase family AAA domain-containing protein 2 (ATAD2) contributes to its anti-TNBC efficacy, which was regulated by EIF3D−ALKBH5 and EIF3D−HIF1α signaling. These findings establish (+)-miliusol as a multifaceted therapeutic candidate and reveal new targets for TNBC treatment.

2. Materials and methods

2.1. Chemistry

2.1.1. Preparation and structural characterization of (+)-miliusol

(+)-Miliusol was obtained as oil from *Miliusa tenuistipitata* W. T. Wang. The molecular formula was determined to be $C_{18}H_{24}O_4$ by HR-ESI-MS that showed a pseudomolecule ion peak at *m*/*z* 305.1746 $[M+H]^+$ (calcd. 305.1747). The characterization of (+)-miliusol was based on NMR (Supporting Information Table S5). ^{1}H NMR (600 MHz, $CDCl_3$), δ(ppm): 6.91−6.89 (1H, dd, J = 10.2, 3.8 Hz), 5.97 (1H, d, J = 10.2 Hz), 5.57 (1H, d, J = 10.1 Hz), 5.14 (1H, d, J = 10.1 Hz), 4.98 (1H, m), 4.56 (1H, m), 3.15 (1H, d, J = 17.3 Hz), 2.30 (1H, d, J = 17.3 Hz), 2.30 (1H, m), 2.20 (1H, dd, J = 14.0, 5.1 Hz), 2.03 (4H, m), 1.70 (3H, s), 1.66 (3H, s), 1.57 (3H, s); ^{13}C NMR (150 MHz, $CDCl_3$), δ(ppm): 196.5, 175.4, 149.0, 145.6, 132.3, 129.0, 123.4, 118.5, 82.3, 63.4, 52.5, 39.8, 39.6, 38.2, 38.2, 26.2, 25.8, 17.8, 17.0.

2.1.2. Synthesis of biotin-(+)-miliusol probe (Scheme 1)

To a solution of 4-pentynoic acid 2 (197.0 mg, 2.0 mmol) and *N*,*N*′-dicyclohexylcarbodiimide (454.0 mg, 2.2 mmol) in dichloromethane (DCM) (10 mL), (+)-miliusol **1** (608.8 mg, 2.0 mmol) and a catalytic amount of 4-dimethylaminopyridine were added. The mixture was stirred at room temperature for 24 h. The mixture was cooled to a temperature of 0 °C, and then the suspension was filtered using a Buchner funnel. The cake was washed with DCM (10 mL). The combined organic layers were subjected to washing with saturated aqueous sodium bicarbonate and brine, followed by drying over anhydrous sodium sulfate. Subsequently, the solvent was evaporated under reduced pressure, and purification was carried out through silica gel flash chromatography (using dichloromethane/methanol 0−4%), resulting in a colorless jelly with a yield of 87%.

(1*R*,7*S*)-1-((*E*)-2,6-Dimethylhepta-1,5-dien-1-yl)-3,10-dioxo-2-oxaspiro[4,5]dec-8-en-7-yl pent-4-ynoate (**3**): ^{1}H NMR (600 MHz, $CDCl_3$), δ(ppm): 6.80 (1H, ddd, J = 10.2, 4.0, 1.1 Hz), 6.07 (1H, dd, J = 10.2, 1.3 Hz), 5.62 (1H, m), 5.46 (1H, d, J = 10.0 Hz), 5.13 (1H, dq, J = 10.1, 1.3 Hz), 5.03−4.95 (1H, m), 3.34 (1H, d, J = 17.6 Hz), 2.67−2.59 (2H, m), 2.58−2.53 (2H, m), 2.41 (1H, ddd, J = 14.7, 4.2, 1.2 Hz), 2.30−2.23 (2H, m), 2.05 (1H, m), 2.03−1.98 (4H, m), 1.69 (3H, d, J = 1.4 Hz), 1.67 (3H, s), 1.58 (3H, s). ^{13}C NMR (150 MHz, $CDCl_3$) 195.07, 174.75, 171.06, 144.88, 144.01, 132.48, 131.21, 123.52, 118.75, 82.05, 81.18, 70.04, 65.64, 52.56, 39.96, 37.29, 36.77, 33.69, 26.32, 26.02, 18.06, 17.19, 14.75.

*2.1.3. Synthesis of biotin-(+)-miliusol (**5**)*

In a solution containing 193.0 mg (0.5 mmol) of probe **3**, tetrahydrofuran (2.0 mL), and water (2.0 mL), NaASe (119.0 mg, 0.6 mmol), $CuSO_4$ (8.0 mg, 0.6 mmol) and intermediate 4 were introduced. The mixture was stirred at room temperature for 24 h, then treated with distilled water (30 mL). The resulting solution underwent three extractions with ethyl acetate (30 mL each). The combined organic layers underwent washing with saturated aqueous sodium bicarbonate and brine, followed by drying over anhydrous sodium sulfate. Subsequently, the solvent was removed under reduced pressure, and purification was carried out using silica gel flash chromatography (dichloromethane/methanol 4%−10%) to yield a white solid at a rate of 57%.

(1*R*,7*S*)-1-((*E*)-2,6-Dimethylhepta-1,5-dien-1-yl)-3,10-dioxo-2-oxaspiro[4,5]dec-8-en-7-yl3-(1-(3-(5-((3a*R*,4*R*,6a*S*)-2-oxohexahydro-1*H*-thieno[3,4-*d*]imidazole-4-yl)pentanamido)propyl)-1*H*-1,2,3-triazol-4-yl)propanoate (biotin-(+)-miliusol, **5**): ^{1}H NMR (600 MHz, $CDCl_3$), δ(ppm): 7.05 (1H, s), 6.82−6.78 (2H, m), 6.52 (1H, s), 6.05 (1H, d, J = 10.2 Hz), 5.61 (m, 1H), 5.41 (1H, d, J = 10.0 Hz), 5.09 (1H, d, J = 10.0 Hz), 4.97(1H, m), 4.52−4.50 (1H, m), 4.38 (1H, t, J = 6.8 Hz), 4.31 (1H, m), 3.33 (1H, d, J = 17.6 Hz), 3.25−3.22 (2H, m), 3.14−3.13 (1H, m), 3.07−3.05 (2H, m), 2.90−2.88 (1H, dd, J = 12.8, 5.0 Hz), 2.81 (2H, t, J = 7.1 Hz), 2.71 (1H, d, J = 12.8 Hz), 2.41−2.38 (1H, dd, J = 14.6, 4.2 Hz), 2.23−2.29 (m), 2.18(2H, t, J = 7.4 Hz), 2.10−2.08 (2H, m), 2.03 (4H, m), 1.73−1.70 (2H, m), 1.66 (6H, s), 1.57(3H, s), 1.43−1.41 (2H, m); ^{13}C NMR (150 MHz, $CDCl_3$), δ(ppm): 194.97, 175.03, 173.99, 171.85, 164.17, 145.82, 144.81, 144.15, 132.27, 130.92, 123.31, 121.92, 118.47, 81.12, 65.27, 61.90, 60.29, 55.83, 52.39, 47.93, 40.75, 39.76, 37.03, 36.47, 36.39, 35.85, 33.67, 30.14, 28.23, 28.07, 26.13, 25.82, 25.68, 20.98. HR-ESI-MS *m*/*z* 711.3518 $[M + H]^+$ (calcd. for $C_{36}H_{51}N_6O_7S$, 711.3534).

2.1.4. Synthesis of PROTAC-(+)-miliusol probe (Scheme 2)

In a solution containing 481.1 mg (1.0 mmol) of VHL ligand (**6**), 158.0 mg (1.1 mmol) of 5-azido-valerianic acid (**7**), and 349.0 μL (2.0 mmol) of *N*,*N*-diisopropylethylamine in DMF (8 mL), HATU (418.0 mg, 1.1 mmol) was added.

The mixture was subjected to stirring at room temperature for a period of 15 h. Following this, it underwent treatment with distilled water (30 mL). The resulting solution was extracted on three occasions with ethyl acetate (30 mL on each occasion). The

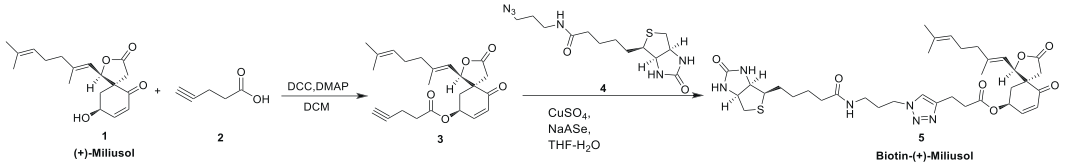

Scheme 1 Synthesis of intermediate **3**.

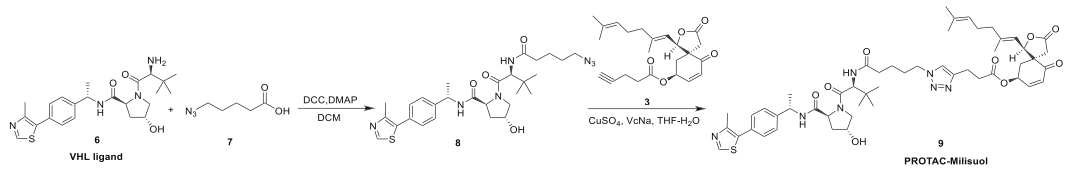

Scheme 2 Synthesis of intermediate **8**.

combined organic layers were then subjected to a thorough washing process using a saturated solution of sodium bicarbonate and brine, followed by a drying step over anhydrous sodium sulfate. Subsequently, the solvent was removed under reduced pressure, and purification was carried out using silica gel flash chromatography (dichloromethane/methanol 1%−10%) to obtain a white solid with a yield of 78%.

(4*R*)-5-((*R*)-2-(5-Azidopentanamido)-3,3-dimethylbutanoyl)-4-hydroxy-*N*-((*S*)-1-(4-(4-methylthiazol-5-yl)phenyl)ethyl)pyrrolidine-2-carboxamide (**8**): ^{1}H NMR (600 MHz, $CDCl_3$), δ(ppm): 8.68 (1H, s), 7.42−7.39 (2H, m), 7.39−7.34 (2H, m), 6.23 (1H, dd, J = 15.9, 8.7 Hz), 5.08 (1H, d, J = 7.1 Hz), 4.72 (1H, td, J = 7.9, 4.2 Hz), 4.56 (1H, dd, J = 8.8, 2.5 Hz), 4.52 (1H, dq, J = 4.2, 2.2 Hz), 4.11 (1H, m), 3.64−3.55 (1H, m), 3.28 (2H, td, J = 6.7, 1.4 Hz), 2.53 (3H, s), 2.25 (2H, m), 2.07 (1H, m), 1.75 (1H, s), 1.73−1.68 (4H, m), 1.63−1.58 (2H, m), 1.47 (3H, d, J = 6.9 Hz), 1.05 (9H, s); ^{13}C-NMR (150 MHz, $CDCl_3$), δ(ppm): 173.28, 172.03, 150.74, 148.33, 143.32, 131.83, 130.80, 129.65, 129.65, 126.58, 126.58, 70.06, 58.76, 57.74, 56.83, 55.64, 48.96, 43.62, 28.36, 26.60, 26.60, 26.60, 22.83, 22.27, 18.68, 17.29, 16.04, 12.62.

2.1.5. Synthesis of PROTAC-(+)-miliusol (*9*)

A solution of probe **3** (193.0 mg, 0.5 mmol) was prepared in a mixture of tetrahydrofuran (2.0 mL) and water (2.0 mL), followed by the addition of NaASe (119.0 mg, 0.6 mmol), $CuSO_4$ (8.0 mg, 0.6 mmol) and intermediate **8**. The mixture was stirred at ambient temperature for 24 h. Following this, it was treated with distilled water (30 mL) and extracted with ethyl acetate (3 × 30 mL). After stirring for a further 15 h at room temperature and adding another 30 mL of distilled water, the resulting solution was extracted three times with 30 mL of ethyl acetate each time. The combined organic layers were washed with saturated aqueous sodium bicarbonate and brine, then dried over anhydrous sodium sulphate. Purification was then carried out using silica gel flash chromatography with a mixture of dichloromethane and methanol in a ratio of 1:10. The resulting white solid was obtained with a yield of 56% after removal of solvents under reduced pressure.

(1*R*,5*S*,7*S*)-1-((*E*)-2,6-dimethylhepta-1,5-dien-1-yl)-3,10-dioxo-2-oxaspiro[4,5]dec-8-en-7-yl-3-(1-(5-(((2*R*)-1-((3*R*)-3-hydroxy-5-(((*S*)-1-(4-(4-methylthiazol-5-yl)phenyl)ethyl)carbamoyl) pyrrolidin-2-yl)-3,3-dimethyl-1-oxobutan-2-yl)amino)-5-oxopentyl)-1*H*-1,2,3-triazol-4-yl)propanoate (PROTAC-Miliusol, **9**): ^{1}H NMR (600 MHz, $CDCl_3$), δ(ppm): 8.67 (1H, s), 7.39 (4H, dd, J = 6.2, 2.1 Hz), 7.36 (2H, d, J = 8.3 Hz), 6.74 (1H, ddd, J = 10.2, 4.0, 1.0 Hz), 6.53−6.47 (1H, m), 6.04 (1H, dd, J = 10.1, 1.3 Hz), 5.54−5.51 (1H, m), 5.34 (1H, d, J = 10.0 Hz), 5.10−5.06 (2H, m), 4.99−4.95 (1H, m), 4.69 (1H, t, J = 8.0 Hz), 4.58 (1H, d, J = 9.0 Hz), 4.49 (1H, d, J = 4.7 Hz), 4.33−4.27 (2H, m), 4.09−4.04 (1H, m), 3.60 (1H, dd, J = 11.3, 3.6 Hz), 3.32 (1H, d, J = 17.7 Hz), 3.05 (2H, td, J = 7.1, 2.5 Hz), 2.83 (2H, q, J = 6.8 Hz), 2.51 (3H, s), 2.48−2.41 (1H, m), 2.37 (1H, dd, J = 14.6, 4.0 Hz), 2.30 (1H, d, J = 17.7 Hz), 2.25 (2H, dt, J = 8.2, 6.4 Hz), 2.19 (1H, dd, J = 14.8, 5.6 Hz), 2.11 (1H, ddd, J = 11.7, 7.8, 4.3 Hz), 2.02 (2H, d, J = 5.6 Hz), 1.98 (2H, d, J = 5.2 Hz), 1.94 (1H, d, J = 33.7 Hz), 1.90−1.85 (2H, m), 1.66 (3H, s), 1.64 (3H, d, J = 1.4 Hz), 1.63−1.58 (2H, m), 1.57 (3H, s), 1.46 (3H, d, J = 6.8 Hz), 1.02 (9H, s); ^{13}C NMR (150 MHz, $CDCl_3$), δ(ppm): 195.17, 175.38, 173.21, 172.23, 172.19, 170.19, 150.69, 148.78, 145.83, 145.05, 144.24, 143.52, 132.46, 131.89, 131.19, 131.14, 129.86, 126.78, 123.52, 121.68, 118.60, 81.31, 70.34, 65.57, 58.79, 57.84, 57.20, 52.57, 50.12, 49.12, 39.96, 37.18, 36.62, 36.11, 35.51, 35.39, 33.95, 30.02, 29.56, 27.79, 26.82, 26.82, 26.82, 26.32, 26.02, 22.60, 22.53, 21.19, 18.07, 17.19, 16.42. HR-ESI-MS *m/z* 954.4793 [M + H] + (calcd. for $C_{51}H_{68}N_7O_9S$, 954.4794).

2.2. Cell culture

The cell lines BT-549, MDA-MB-231, MDA-MB-436, MDA-MB-468, HCC1937, MCF-7, 4T1, MGC803, HGC-27, A549, PANC-1, HCT116, HepG2, MCF-10A, GES-1, BEAS-2B, hTERT-HPNE, NCM460, and L-O2 were obtained from ATCC. BT-549, HCC1937, A549, MCF-10A, GES-1, NCM460 and L-O2 were maintained in RPMI-1640 medium supplemented with 10% (*v*/*v*) fetal bovine serum, streptomycin (50 U/mL) and penicillin (50 U/mL). MDA-MB-231, MDA-MB-436, MDA-MB-468, MCF-7, 4T1, MGC803, HGC-27, PANC-1, HCT116, HepG2, BEAS-2B and hTERT-HPNE maintained in DMEM medium supplemented with 10% (*v*/*v*) fetal bovine serum, streptomycin (50 U/mL) and penicillin (50 U/mL). The cells were cultured at 37 °C with 5% CO_2 in an incubator.

2.3. Antibodies and reagents

The antibodies used in this study were as follows: hexokinase II (HK II) (2867, CST), glucose transporter 1 (Glut1) (73015, CST), lactate dehydrogenase A (LDHA) (3582, CST), matrix metallopeptidase 2 (MMP-2) (40994, CST), lactate dehydrogenase B (LDHB) (14824-1-AP, Proteintech), β-actin (3700, CST), BCL2-associated X (Bax) (14796, CST), B-cell lymphoma-2 (Bcl-2) (15071, CST), Caspase-3 (9662, CST), epithelial cadherin (E-Cadherin) (14472, CST), Caspase-8 (9746, CST), Caspase-9 (9504, CST), sequestosome-1 (SQSTM1/p62) (23214, CST), autophagy-related gene 5 (ATG5) (12994, CST), microtubule-associated protein 1 light chain 3 beta (LC3B) (3868, CST), Beclin-1 (3495, CST), PAK1 (2602, CST), Phospho-PAK1$^{(Ser144)}$ (2606, CST), phospho-PAK1$^{(Ser199/204)}$ (2605, CST), ATAD2 (50563, CST), c-Myc (13987, CST), phospho-c-Raf$^{(Ser338)}$ (9427, CST), phospho-MEK1/2$^{(Ser217/221)}$ (3958, CST), phospho-MEK1/2$^{(Ser298)}$ (98195, CST), lysosome-associated membrane protein 2 (LAMP2) (34141, CST), PARP (9532, CST), eIF3D (40765, CST), ribosomal protein S5 (RPS5) (16964-1-AP, Proteintech), 40S ribosomal protein S16 (RPS16) (15603-1-AP, Proteintech), c-Jun (9165, CST), ALKBH5 (49015, CST),

GLUT4(2213, CST), Tumor-specific pyruvate kinase M2 (PKM2) (4053, CST), RUVBL1 (12300, CST), β-catenin (8480, CST), heat shock protein 90 (HSP90) (4877, CST), phospho-Akt$^{(Ser473)}$ (4060, CST), Akt (9272, CST), Mammalian target of rapamycin (mTOR) (2983, CST), phospho-mTOR$^{(Ser2448)}$ (5536, CST), PERK (5683, CST), Unc-51-like kinase 1 (ULK1) (8054, CST), phospho-p44/42 MAPK (Erk1/2) $^{(Thr202/Tyr204)}$ (4370, CST), phospho-ULK1$^{(Ser757)}$ (14202, CST), phospho-ULK1$^{(Ser555)}$ (5869, CST), focal adhesion kinase family interacting protein of 200 kDa (FIP200) (12436, CST), autophagy-related protein 101 (Atg101) (13492, CST), CHOP (2895, CST), phospho-Atg13$^{(Ser355)}$ (46329, CST), inositol-requiring enzyme 1 alpha (IRE1α) (3294, CST), X-box-binding protein-1 (XBP-1s) (40435, CST), Snail (3879, CST), autophagy-related protein 13 (Atg13) (13468, CST), Ki-67 (9449, CST), SAPK/JNK (9252, CST), Caspase-12 (35965, CST), phospho-SAPK/JNK$^{(Thr183/Tyr185)}$ (9255, CST).

Other reagents include 3-methyladenine (3-MA) (M9281, Sigma−Aldrich), chloroquine (CQ) (C6628, Sigma−Aldrich), DAPI (D9542, Sigma−Aldrich), Actin-Tracker Red-555 (C2203S, beyotime), 2-NBDG (ab235976, Abcam), D-Lactate Assay Kit (Colorimetric) (ab83429, Abcam), Lactate Dehydrogenase Activity Detection Kit (C0016, beyotime), One-step TUNEL Cell Apoptosis Detection Kit (Red fluorescence) (C1089, beyotime), Annexin V-FITC/PI Apoptosis Detection Kit (FXP018-100, 4A Biotech), and SignalSilence® PAK1 siRNA (6361, CST). si-ATAD2 and si-EIF3D were purchased from GENE (Shanghai, China). RFP-GFP-LC3 adenovirus was purchased from Hanbio (Shanghai, China). MG-132 (HY-13259, MCE) was purchased from MedChemExpress (Shanghai, China). 3-Bromopyruvic acid (3-BP) (HY-19992, MCE) was purchased from MedChemExpress (Shanghai, China). MedChemExpress (Shanghai, China) provides the compound known as Dorsomorphin (Compound C) (HY-13418A, MCE).

2.4. Pharmacophore-based virtual screening

To obtain a pharmacophore capable of screening for Warburg effect inhibitors, four compounds (bis-geranylacylphloroglucinol derivative moronone[18], Compound **3**[19], Compound **17**[19] and SRI-37683[20]) were selected as training set to build the pharmacophore models. The attributes of Principal (set to a value of 2) and MaxOmitFeat (set to a value of 0) were added to all the molecules in the training set. The pharmacophore characteristic elements include hydrophobic, hydrogen bond (HB) acceptor, HB donor and ring aromatic elements. First, all possible pharmacophore feature mappings and features for the selected training set were computed by the Feature Mapping protocol of DS2016 to produce 10 pharmacophores. A validation program was conducted by the Ligand Profiler protocol to verify the ability to predict the active compounds of each pharmacophore model. The validation process involved evaluating the mapping of each pharmacophore based on each molecule, which in turn generated the relevant heat map. A pharmacophore model with a high score for decoy set was considered the candidate pharmacophore, and applied to the follow-up virtual screening. The top ten compounds were found according to the Fit values pharmacophore-based screening.

2.5. Molecular docking

The molecular docking of (+)-miliusol into EIF3D (PDB code 6YBS) was conducted using Discovery Studio 3.5 software, with the active binding site defined based on predicted activity and a radius of 8.5 Å considered. The protein structure underwent processing including hydrogen atom addition, water removal, and Charmm forcefield assignment. The gold score was selected as the scoring function while maintaining default settings for other parameters. A maximum of 30 conformations were generated to preserve ligand poses with a minimum RMSD between final poses set at 0.50 Å. The protein structure used in this study was obtained from PDB databank (https://www.rcsb.org)[21].

2.6. MS-CETSA

The MS-CETSA assay was performed as previously described[22,23]. BT-549 cells were harvested, washed with pre-cold PBS, and resuspended in lysis buffer. The lysate was then treated with (+)-miliusol, heated, and centrifuged to collect the supernatant. Proteins were reduced and alkylated before digestion with LysC and trypsin. The digested peptides were labeled with TMT-10plex reagents, desalted, fractionated by high pH reversed phase HPLC, and analyzed by LC−MS/MS.

2.7. RNA-sequencing (RNA-seq) analysis

The (+)-miliusol treated xenografts and controls were subjected to TRIzol Reagent (Invitrogen, USA) for total RNA extraction, followed by quantification using NanoDrop (Thermo Fisher Scientific, USA). The HiSeq X Ten instrument (Illumina, Huada Gene, Wuhan, China) was utilized for RNA-seq analysis. To eliminate low-quality bases, the obtained data underwent quality trimming with Cutadapt version 1.9.1 before aligning them to the human genome (*Mus musculus*. GRCm38) downloaded from the NCBI database. DESeq2 version 1.6.3 was employed for differential mRNA expression analysis with a significance threshold of adjusted P-value <0.05 applied to identify genes showing at least a two-fold change in expression[24].

2.8. Quantitative proteomics

A total of 200 μL of SDT protein cleavage solution was added to each sample, which was then shaken thoroughly. We heated the mixture at 100 °C for 5 min, followed by ultrasound treatment on ice for 5 min. The process of centrifugation at 13,000 × g was carried out for a duration of 30 min, after which the resulting filtrate was transferred into a tube equipped with a 0.22-micron pore size filter membrane. BCA quantification was performed using only 1 μL of the filtrate and the remaining portion was stored at −80 °C. FASP processing involved taking 300 μg from each sample, which were then treated with 100 mmol/L DTT (final concentration), cooked at 100 °C for 5 min before adding UA buffer and thorough mixing. The resulting mixture was transferred to an ultrafiltration tube and centrifuged at RT before discarding the filtrate. The process was repeated three times. After that, the samples were treated with IAA in UA buffer, incubated at room temperature to avoid light exposure, and then centrifuged under the same conditions three times. Finally, trypsin buffer totaling to a volume of 52 μL was added before being placed on a constant temperature homogenizer for digestion.

2.8.1. SDS-PAGE

20 μg protein samples were mixed with 5 × loading buffer. The ratio of the samples was 5:1 (*v*/*v*). The buffer composition was as follows: 250 mmol/L Tris-HCl (pH 6.8), 10% (*w*/*v*) SDS, 0.5% (*w*/

v) BPB, 50% (*v*/*v*) glycerol and 5% DTT. The samples were subjected to a heating process in a boiling water bath for a duration of 5 min. Following this, the samples were then subjected to a centrifugation process in order to collect the upper layer for electrophoresis in a 12% SDS-PAGE gel. The gel was then subjected to an electric current of 150 V for a duration of 45 min. At the end of electrophoresis, the colloid was cleaned slightly with deionized water, and then stained.

2.8.2. MS-CETSA

The LC−MS/MS analysis was performed using an EASY-nLC 1200 system connected to an Orbitrap Eclipse Tribrid mass spectrometer equipped with a nanoelectrospray source. 500 ng of peptides in 0.1% formic acid and 2% acetonitrile were loaded onto an Acclaim PepMap 100 C18 Nano Trap Column and separated on an Acclaim PepMap RSLC C18 column using specific gradients. MS1 data were collected at a resolution of 120,000 with a scan range of *m*/*z* 400−1200, while MS/MS spectra were acquired at a scan range of *m*/*z* 200−1200. The precursors were isolated by Quadrupole and fragmented with a collision energy of 36%, detected in IonTrap. FAIMS device was set between the nanoESI source and the Orbitrap Eclipse for LC−MS/MS analysis.

2.8.3. Quantitative proteomics

Solvent A contained 0.1% formic acid in water, while Solvent B contained 0.1% formic acid in 100% acetonitrile. The Thermo Scientific analytical column used had dimensions of 75 μm × 25 cm, with a particle size of 5 μm and a pore size of 100 Å, coated with C18 material. Prior to the experiment, the column was conditioned using a mixture consisting of 95% solvent A. Samples were loaded into a Thermo Scientific EASY trap column and separated by column chromatography. After capillary high performance liquid chromatography desalting and separation, the enzymatic hydrolysis products were analyzed by Orbitrap-Fusion mass spectrometer (Thermo Finnigan, San Jose, CA, USA). Analysis duration: 60 min were allocated for the analysis process.

2.8.4. Mass spectrum database search and analysis

The mass spectrometry analysis used RAW files as the raw data and Proteome Discoverer 2.4 (Thermo Scientific) with its built-in software Sequest for database identification and quantitative analysis. The selected database was Uniprot-20230131-human-207393.fasta, containing a total of 207,393 sequences. Proteome Discoverer 2.4 screened for peptide identification results with FDR$\leq$0.01 (high confidence) and conducted quantitative analysis based on ion peak intensity values of peptides, followed by median homogenization across all channels to generate final protein quantification results.

2.9. Cell viability assay

The cells were seeded into 96-well plates at a density of 6000 cells per well and left to adhere for 24 h. Following this stabilization period, test compounds were administered at specified concentrations and exposure times. Cell viability was subsequently quantified using MTT assays, with absorbance measurements normalized to untreated controls.

2.10. Glucose uptake assay

The uptake of cellular glucose was assessed by flow cytometry to measure the uptake of 2-NBDG, as previously outlined[25]. In brief, the treated cells were exposed to 50 μmol/L 2-NBDG for 30 min at 37 °C. Following washing and resuspension in pre-cooled PBS, fluorescence intensity at 488 nm was measured using a flow cytometer.

2.11. Lactate production assay

BT-549 and MDA-MB-231 cells were seeded at a density of 200,000 cells per well in 6-well plates. They were then treated for 24 h, followed by measuring lactate production using the D-Lactate Assay Kit. The study assessed lactate production relative to protein levels and normalized it to the control group treated with DMSO. Additionally, cellular lactate dehydrogenase (LDH) activity was determined using the Lactate Dehydrogenase Activity Detection Kit.

2.12. Extracellular acidification rate (ECAR) and oxygen consumption rate (OCR)

2.12.1. Cell seeding and treatment

A single-cell suspension (1×10^5 cells/mL) should be prepared in complete medium. Add 100 μL to each well of a 96-well plate and incubate at 37 °C for 24 h. Next, treat the cells with (+)-miliusol for a further 24 h, and then centrifuge them at 300 × *g* for 5 min. Proceed with subsequent assays.

2.12.2. Medium exchange and preparation

Aspirate 175 μL of spent medium from each well. Wash twice with 600 μL of hippocampus-specific assay medium, then add 450−525 μL of fresh medium per well. Verify cell monolayer integrity by phase-contrast microscopy. Transfer plates to a non-CO_2 incubator and equilibrate for 1 h at 37 °C.

2.12.3. Reagent administration

Prepare respiratory chain inhibitor cocktail containing: Oligomycin (1 μmol/L); FCCP (1 μmol/L); Antimycin A (1 μmol/L). Add 75 μL of inhibitor solution to designated reagent wells according to experimental design.

2.12.4. Instrument calibration

Perform system calibration using manufacturer-recommended protocols. Verify proper function of all sensors and fluidics. Run calibration plate according to standard operating procedures.

2.12.5. Assay execution

Replace calibration plate with cell culture plate. Initiate assay protocol with predefined measurement intervals and parameters. Monitor real-time data acquisition for quality control.

2.13. Transfection of siRNA

The BT-549 and MDA-MB-231 cells were subjected to transfection with si-PAK1, si-ATAD2, and a negative control siRNA (si-NC) at a concentration of 50 nmol/L using Lipofectamine 3000 reagent (Invitrogen) in accordance with the manufacturer's instructions. Subsequent experiments were conducted 48 h post-transfection.

2.14. Apoptosis assay

The BT-549 and MDA-MB-231 cells were exposed to varying concentrations of (+)-miliusol, 3-MA, or CQ. The assessment of cell apoptosis was conducted through the utilisation of the Terminal-deoxynucleoitidyl Transferase Mediated Nick End Labeling (TUNEL) assay, a method employed to quantitate DNA fragmentation. Furthermore, the Annexin-V/PI double staining assay was employed to ascertain the proportion of cell apoptosis in both the early and late stages. JC-1 staining was utilised to detect changes in mitochondrial membrane potential in TNBC cells treated with (+)-miliusol.

2.15. Cell migration assay

The migratory ability of cells was evaluated using the wound healing and Transwell assays as previously outlined[24]. In brief, BT-549 and MDA-MB-231 cells were seeded in 6-well plates for the wound healing assay. Upon reaching full confluence in culture, the cells were gently scratched with a 1 mL pipette tip. These initial cellular wounds were immediately documented using a microscope after the removal of floating cells. Then various drugs are used for treatment.

Then allow the scratch to heal in the medium without FBS for 24 or 48 h. Record the scratch under a microscope and use ImageJ software to quantify its degree.

In the Transwell assay, the initial step involves the resuspension of 20,000 BT-549 or MDA-MB-231 cells in FBS-free medium. Subsequently, 200 μL of the cell suspension is inoculated into the upper chamber of the Transwell apparatus. The addition of 600 μL of drug-containing cell culture medium, which has been supplemented with 10% foetal bovine serum (FBS), to the lower chamber is required, followed by incubation at 37 °C for a period of 24 h. After that, the top layer cells were removed with a swab and the bottom layer cells were fixed with 4% paraformaldehyde for 30 min at room temperature. Subsequently, the lower layer cells were stained with crystal violet and photographed.

2.16. Autophagy assay

BT-549 and MDA-MB-231 cells were transfected with GFP/mRFP-LC3 for 24 h and subsequently treated with (+)-miliusol for another 24 h. Cells were harvested afterwards, and the fluorescence intensity of GFP and RFP was measured by flow cytometry. In addition, immunofluorescence for LC3 and LAMP2 was used in this study to detect the process of autophagy.

2.17. Colony formation assay

The cells were placed into 6-well dishes and exposed to medication for a period of two weeks. Subsequently, the cells were immobilized using 4% paraformaldehyde for a period of half an hour, after which they were subjected to staining with crystal violet.

2.18. Western blot-coupled cell thermal shift assay (WB-CETSA assay)

The interaction of (+)-miliusol with the protein target was detected using the WB-CETSA. Specifically, cells were treated with DMSO or (+)-miliusol for 6 h. Cells were collected and then heated for 3 min at a temperature gradient of 37−67 °C and subjected to three freeze−thaw cycles and centrifuged at 12,000 rpm and 4 °C for 20 min. A Western blot was then carried out as a follow-up to detect the protein thermal stability changes.

2.19. Biotin-(+)-miliusol pulldown assay

Streptavidin-agarose beads were incubated with biotin-(+)-miliusol in HEPES buffer for 2 h at 25 °C. BT-549 and MDA-MB-231 cell lysates were then incubated with the biotin-(+)-miliusol−streptavidin complex overnight at 4 °C. Proteins bound to the beads were analyzed by WB using an EIF3D antibody after washing with HEPES buffer.

2.20. Western blot

BT-549 and MDA-MB-231 cells were exposed to varying concentrations of (+)-miliusol for specified time periods, followed by collection. Cell lysis was performed using the cell lysis buffer from the Western and IP Kit (Beyotime, P0013) for 1 h. The protein content in the supernatant after centrifugation at 12,000 rpm for 20 min was determined using the BCA Protein Concentration Determination Kit (P0011, Beyotime). Thereafter, an equivalent quantity of denatured protein was separated on an SDS-polyacrylamide gel (SDS-PAGE), following which the gel was transferred onto a polyvinylidene fluoride (PVDF) membrane. The membranes were blocked with 5% skimmed milk at room temperature for 1 h, followed by overnight incubation with the primary antibody at 4 °C. After washing with TBST, HRP-conjugated secondary antibodies were applied to the membranes. Visualization of protein bands was achieved through enhanced chemiluminescence detection, and ImageJ was used to quantify grayscale values of the bands.

2.21. Immunofluorescence analysis

The BT-549 and MDA-MB-231 cells were sequentially exposed to Ki-67 antibody (1:200), LDHA antibody (1:200), MMP-2 antibody (1:200), E-cadherin antibody (1:200), LC3 antibody (1:200), LAMP2 antibody (1:200), ATAD2 antibody (1:200), PAK1 antibody (1:200), p-ERK1/2$^{Thr202/Tyr204}$ antibody (1:200), XBP-1s antibody (1:200) and JNK12 antibody (1:200) at 4 °C overnight. The antibodies were diluted in PBS containing 10% BSA, followed by incubation with fluorescent-labeled secondary antibodies for 60 min at room temperature.

2.22. Zebrafish tumor xenograft model

The wild-type zebrafish (strain AB) was obtained from Hangzhou Hunter Biotechnology Co., Ltd. (Hangzhou, China) and was maintained under standard conditions at 28 °C in a 14-h:10-h light-dark cycle[26]. Each wild-type zebrafish embryo was transplanted with 200 CM-DIL marked BT-549 or MDA-MB-231 cells 48 h after fertilization using a microsyringe IM-300 after anesthesia. After injection, the embryos were incubated at 28 °C for 1 h and then at 35 °C. Two hundred xenografted zebrafish embryos tagged with CM-DIL and either BT-549 or MDA-MB-231 were randomly selected and inoculated into 10 replicates of 6-well plates, with 30 embryos per well. After incubation with (+)-miliusol (2.0 μg/mL) at 35 °C for 5 days, 10 of the 30 embryos were randomly selected from each well and visualized under a fluorescent microscope. The fluorescence intensity of the zebrafish abdomen inoculated with BT-549 or MDA-MB-231 was

assessed to determine the inhibitory effect of (+)-miliusol on growth. The total distance of metastasis in the tail of xenograft zebrafish implanted with BT-549 or MDA-MB-231 was measured to evaluate the impact of (+)-miliusol on cell metastasis.

2.23. Mice models

2.23.1. Xenograft mouse model

Female BALB/c nude mice weighing 18 to 20 g were purchased from SPF (Beijing, China) Biotechnology Co., Ltd. (certificate no. SCXK [Jing] 2019-0010). All animal procedures were approved by Shenzhen University Medical Department Laboratory Animal Ethics Committee (No: A202401678). Following acclimatisation, the mice were subcutaneously injected with BT-549 cells and MDA-MB-231 cells (5×10^6 cells/mouse). As the tumour volume increased to approximately 0.1 cm^3, the subjects were randomly divided into four groups, with each group consisting of six to eight subjects. BT-549 xenograft mouse: the control group, 10 mg/kg (+)-miliusol-treated group, 20 mg/kg CQ-treated group and 10 mg/kg (+)-miliusol-treated + 20 mg/kg CQ-treated group. MDA-MB-231 xenograft mouse: the control group, 8 mg/kg (+)-miliusol-treated group, 20 mg/kg CQ-treated group and 8 mg/kg (+)-miliusol-treated + 20 mg/kg CQ-treated group. The mice were weighed daily during dosing (intraperitoneal injection, daily), and the tumor size was measured daily with an electronic vernier caliper. Last day of the experiment, the animals were anesthetized with isoflurane, then mice were euthanized by cervical dislocation, and tumor tissue was harvested and subjected to liquid nitrogen or formalin for subsequent analyses.

For the *in vivo* cancer cell metastasis experiment of TNBC cells, 1×10^5 cells (MDA-MB-231-LUC or BT-549-LUC) were injected into nude mice through the tail vein injection, and administration began on Day 2 after injection, and images were collected on Days 0, 4, 8, 12 and 16, respectively. The mice were euthanized on the 24th day of administration, and their organs were subsequently harvested. Moreover, blood and spleen tissues were subjected to flow cytometry to quantify CD45, CD3, and CD19 markers, thereby assessing B cell and T cell populations.

2.23.2. BALB/c mouse model

To investigate the toxicity of (+)-miliusol, female BALB/c mice were administered (+)-miliusol daily for a period of 14 days. Following the treatment, blood samples were collected for comprehensive hematological analysis. Major organs were harvested for HE staining. Additionally, blood, spleen, and thymus tissues were subjected to flow cytometry to quantify CD45, CD3, and CD19 markers, thereby assessing B cell and T cell populations.

2.24. Survival curve

The subcutaneous injection of 100 μL of phosphate-buffered saline (PBS) containing 5×10^6 BT-549 cells/MDA-MB-231 cells or 5×10^4 4T1 cells should be performed into the right inguinal mammary fat pad of female BALB/c mice aged 4−6 weeks. As the tumor volume increased to approximately 0.1 cm^3, the subjects were randomly divided into four groups, with each group consisting of ten subjects. The 4T1 transplanted tumour mouse model comprised the following groups: the control group, the (+)-miliusol-treated group at 10 mg/kg (or 8 mg/kg), the CQ-treated group at 20 mg/kg, and the combination of 10 mg/kg (or 8 mg/kg) (+)-miliusol-treated and 20 mg/kg CQ-treated groups. The mouse was euthanised when the tumor diameter exceeded 15 mm or when the mouse was moribund during the observation period. The time of euthanasia was recorded as the time of death.

2.25. Immune cells were analyzed by flow cytometry

2.25.1. Preparation of single-cell suspension from peripheral blood of mice

Peripheral blood samples should be collected from mice in tubes containing an anticoagulant. The addition of 100 μL of fresh blood to a centrifuge tube is the first step in the procedure. This is followed by the addition of one test-specific flow cytometry antibody. The mixture should be thoroughly agitated and then incubated at a temperature of 4 °C in conditions of darkness for a period of 30 min. Following this, 2−5 mL of 1 × red blood cell lysis buffer should be added, and the mixture thoroughly agitated. The samples are then to be lysed at 4 °C for 5 min. Centrifugation at 300 × *g* for 5 min is required to yield the cell sediment, with the supernatant being discarded. The object should then be washed once with phosphate buffered saline (PBS). The cells should then be resuspended in 400 μL of cell staining buffer, after which they can be analysed using a flow cytometer.

2.25.2. Preparation of single-cell suspensions of tumor tissues

After completely removing the tumor, transfer it to a 1.5 mL centrifuge tube and mince it thoroughly. Then, transfer the tumor tissue suspension to a 50 mL centrifuge tube. Add 9 mL of PBS, resuspend the cell pellet and add 1 mL of 10 × Triple Enzyme Stock Solution. The contents should then be gently pipetted to ensure thorough mixing, after which the mixture should be incubated at 37 °C in a water bath shaker for a period of 1−2 h. Following digestion, the solution should be diluted with PBS and passed through a 75-micron mesh filter to remove any residual tissue fragments. Subsequently, the subject should be washed once with PBS. The cell suspension should then be collected and subjected to a centrifugal process at a speed of 300 × *g* for a duration of 5 min. The superior portion should be discarded. The cells must then be resuspended in cell staining buffer, with the concentration adjusted to 1×10^7 cells/mL, prior to staining and detection.

2.26. Immunohistochemistry analysis

Tumor tissues were collected, fixed with 4% paraformaldehyde and embedded in paraffin. The samples were then sectioned to a thickness of 5 μm and subsequently affixed onto slides. Following this, they were washed and antigen repaired with EDTA. The following day, the samples were subjected to an overnight incubation with primary antibodies at 4 °C. Sections were then rinsed with phosphate buffer and incubated with secondary antibody for 1 h at room temperature. Finally, the sections were washed and reacted with a diaminobenzidine chromogenic solution for 5 min. Sections were subjected to staining with hematoxylin, followed by thorough washing, dehydration, and subsequent coverage with cover glasses. The results of the staining were obtained using a microscope.

2.27. Statistical analysis

All experiments were conducted independently at least three times, and the data are expressed as mean ± standard error of mean (SEM). Statistical analysis was carried out using GraphPad

Prism 8.0 software, with one-way ANOVA and Student's *t*-test used for comparisons. A significance level of $P < 0.05$ was applied.

3. Results

3.1. Identification of (+)-miliusol as a novel Warburg effect inhibitor

In order to discover novel natural small molecules with inhibitory effect on the Warburg effect, we adopted a strategy which combines data mining, bioinformatics analysis, artificial intelligence screening and experimental verification, and successfully identified (+)-miliusol as a potent inhibitor of Warburg effect in TNBC.

We first carried out data mining and curated a collection of 96 small molecules from the PubMed database, which have been shown to have the capability of modulating the Warburg effect of cancer cells (Supporting Information Table S1). Subsequently, the Swiss Target Prediction database was utilized to predict potential targets of these compounds [27], and the Gene Ontology (GO) biological process enrichment analysis was further conducted on these targets using the DAVID database[28]. Compounds whose predicted targets exhibited significant enrichment in the Warburg pathway were then screened out, with four compounds selected as the training set (Supporting Information Table S2) and another five compounds used as the decoy set (Supporting Information Table S3). 10 pharmacophore models were established using the training set. After the validation using the decoy set, Model 2 was selected as the optimal one (Supporting Information Fig. S1). Then, we performed pharmacophore-based virtual screening from a natural product database consisting of 21,388 compounds from Topscience Co. Ltd., and 2008 compounds from an in-house compound library revised by Lipinski's rule of five and Veber's rule. By assessment of the pharmacophore features, shapes, and exclusion constraints, the ligand database was mapped into the pharmacophore model and ten ligands were selected with a criterion of Fitvalue >3.3. Among the ten candidates, (+)-miliusol showed the highest score and the most promising Warburg pathway-interfering potential (Fig. 1A, Supporting Information Fig. S1 and Table S4).

Next, we tested whether (+)-miliusol showed anti-tumor activity in TNBC cells. Results of MTT assay indicated that (+)-miliusol exhibited significant suppressive functions on cell proliferation of BT-549 (6 h IC_{50} = 5.443 ± 0.736 μmol/L; 12 h IC_{50} = 5.862 ± 0.768 μmol/L; 24 h IC_{50} = 4.85 ± 0.686 μmol/L; 36 h IC_{50} = 3.396 ± 0.531 μmol/L; 48 h IC_{50} = 3.043 ± 0.483 μmol/L) and MDA-MB-231 (6 h IC_{50} = 21.906 ± 1.341 μmol/L; 12 h IC_{50} = 11.885 ± 1.075 μmol/L; 24 h IC_{50} = 4.185 ± 0.622 μmol/L; 36 h IC_{50} = 4.692 ± 0.671 μmol/L; 48 h IC_{50} = 4.684 ± 0.671 μmol/L) (Fig. 1B and C). Among a panel of TNBC cell lines, BT-549 exhibited the highest sensitivity to (+)-miliusol treatment, as determined by dose-response profiling. Notably, (+)-miliusol demonstrated broad-spectrum anti-proliferative activity across multiple cancer cell types, with IC_{50} values varying by cell lineage. Strikingly, (+)-miliusol exhibited more potent anti-tumor activity in cancer cells compared to normal cells, suggesting a favorable therapeutic window and potential safety profile for (+)-miliusol in cancer therapy (Supporting Information Fig. S2). Later, BT-549 and MDA-MB-231 cells were chosen for follow-up investigations. Results of colony formation assay revealed that (+)-miliusol exhibited inhibitory effects on the long-term proliferation ability of BT-549 and MDA-MB-231 cells (Fig. 1D and E). Results of 3D cell spheroid formation assay further demonstrated that (+)-miliusol could inhibit the formation of TNBC tumor spheroid in a concentration-dependent manner (Fig. 1F and G), thereby confirming the compound's ability to disrupt collective tumor cell growth in a physiologically relevant model system. The expressions of the proliferation markers Ki-67 and EdU in (+)-miliusol-treated BT-549 and MDA-MB-231 cells were also quantified by immunofluoresent staining. Results revealed that the fluorescence intensity of Ki-67 and EdU decreased upon the treatment of (+)-miliusol in a concentration-dependent manner, suggesting that (+)-miliusol could dose-dependently inhibit the proliferation of BT-549 and MDA-MB-231 cells (Fig. 1H−K), consistent with the observed suppression of clonogenic and spheroid-forming capacity. Collectively, these results illustrate that (+)-miliusol is a candidate compound with potent *in vitro* anti-tumor activity in TNBC.

3.2. (+)-Miliusol inhibits the Warburg effect and cell migration in TNBC cells

In order to verify the potential inhibitory effect of (+)-miliusol on the Warburg effect in TNBC cells, the effect of (+)-miliusol on the glucose uptake capacity and lactate production activity was first evaluated. These are key indicators of the Warburg effect, as previously defined[29]. The results demonstrated that (+)-miliusol exerted a dose-dependent inhibitory effect on glucose uptake (Fig. 2A and B) and lactate production (Fig. 2C and D) in both BT-549 and MDA-MB-231 cells. Treatment with (+)-miliusol also decreased the fluorescent intensity of LDHA, a crucial rate-limiting enzyme in aerobic glycolysis[9], in BT-549 cells and MDA-MB-231 cells (Fig. 2E and G). Besides, the cellular LDH activity also showed a remarkable attenuation upon the treatment with (+)-miliusol (Fig. 2F and H), indicating a profound metabolic perturbation in TNBC cells. Next, the expression of HK II, a key enzyme in glycolysis and crucial for the Warburg effect, was examined by immunofluorescence staining analysis[30]. As shown in Fig. 2I and J, HK II exhibited high expression patterns and cytoplasmic distribution in TNBC cells. After treatment with (+)-miliusol, the expression level of HK II significantly decreased, particularly in BT-549 cells, coinciding with the observed attenuation of LDH activity. This dual suppression of rate-limiting glycolytic enzymes (HKII and LDH) suggests (+)-miliusol disrupts the Warburg effect. Next, the expressions of a panel of key glycolysis regulators were evaluated by immunoblotting, including HK II, GLUT1, LDHA, and LDHB (Fig. 2K, Supporting Information Fig. S3A−S3D). Results demonstrated that (+)-miliusol inhibited the glycolysis in TNBC cells by down-regulating key glycolysis regulators, including GLUT1, HK II, LDHA, and LDHB. To delineate the metabolic consequences of (+)-miliusol treatment, we performed real-time bioenergetic profiling through OCR and ECAR measurements. The results demonstrated that (+)-miliusol significantly suppressed glycolysis, glycolytic reserve, and glycolytic capacity in TNBC cells. Additionally, treatment with (+)-miliusol markedly reduced basal respiration, ATP production, maximal respiration, and spare respiratory capacity (Fig. 2L−O). These results further confirm that (+)-miliusol strongly inhibits the Warburg effect in TNBC cells, leading to mitochondrial metabolic disruption and energy supply collapse in TNBC cells.

High metastatic potential is a prominent feature of TNBC, and aerobic glycolysis is a key player of this feature[31]. Therefore, we next investigated whether the treatment of (+)-miliusol could

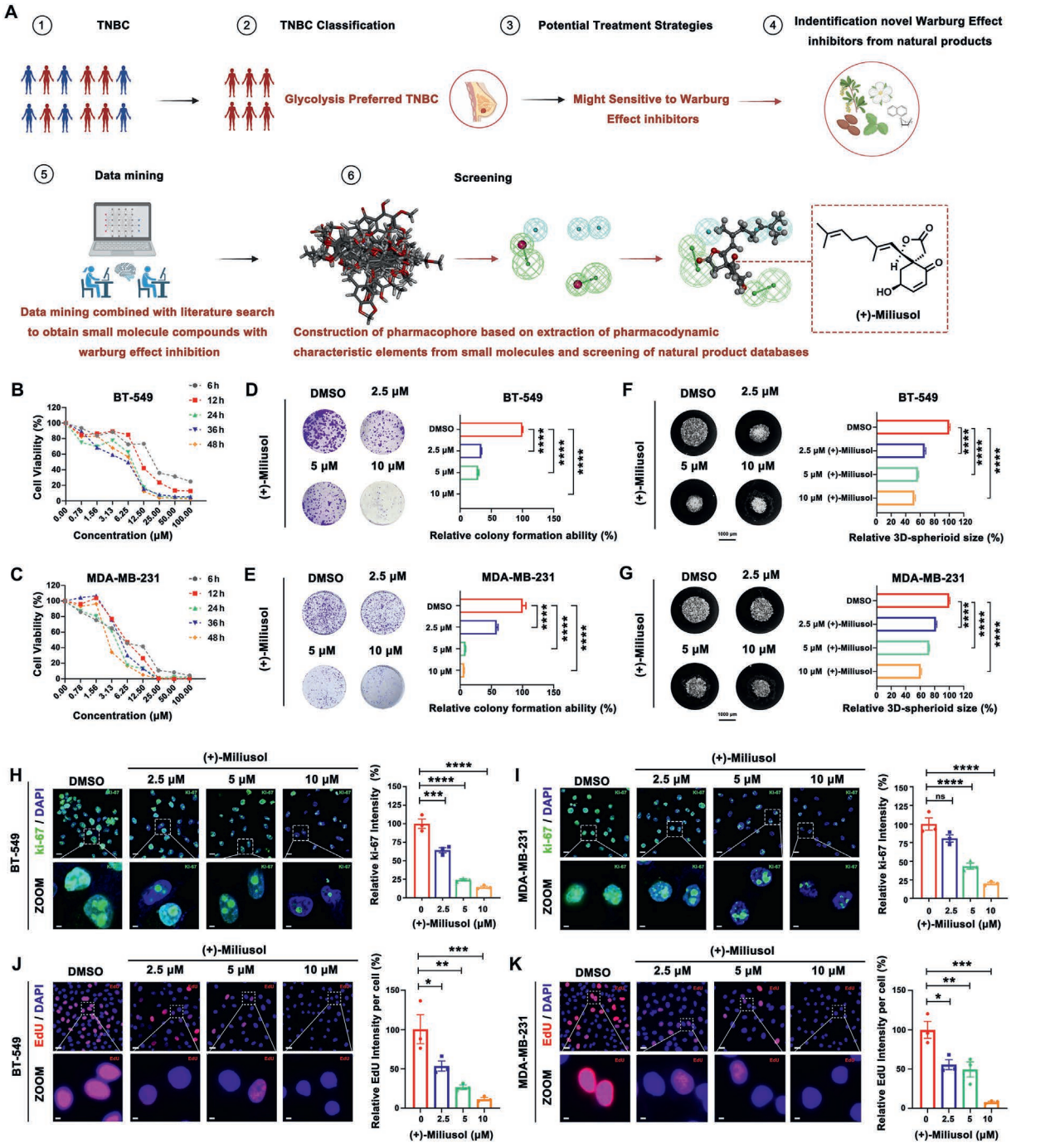

Figure 1 Identification of (+)-miliusol as a glycolysis inhibition candidate in TNBC from natural products. (A) Flowchart of screening for (+)-miliusol in glycolysis-preferred TNBC. (B, C) MTT assay detection of the cell viability of (+)-miliusol treatment (100, 50, 25, 12.5, 6.25, 3.13, 1.56, and 0.78 μmol/L) for 6, 12, 24, 36 and 48 h, respectively. (D, E) Colony formation ability of (+)-miliusol (2.5, 5, and 10 μmol/L) treatment of BT-549 and MDA-MB-231 cells. (F, G) Effect of (+)-miliusol (2.5, 5, and 10 μmol/L) on 3D-spheroid formation in BT-549 and MDA-MB-231 cells. (H, I) Immunofluorescence detection of Ki-67, a cell proliferation marker, following treatment with (+)-miliusol at concentrations of 2.5, 5, and 10 μmol/L. Scale bar = 10 μm. ZOOM Scale bar = 2 μm. The fluorescence intensity of Ki-67 was calculated using Image J software. (J, K) EdU assay of (+)-miliusol (2.5, 5, and 10 μmol/L) on TNBC cell proliferation. Scale bar = 10 μm. ZOOM Scale bar = 2 μm. Data are presented as mean ± SEM, $n = 3$. ns, no significance; *$P < 0.05$; **$P < 0.01$; ***$P < 0.001$; ****$P < 0.0001$, compared with the DMSO treated group. M, mol/L.

exerts any effects on TNBC cell migration. The results of the wound healing assay demonstrated that (+)-miliusol effectively suppresses TNBC cell migration (Supporting Information Fig. S4A). Consistently, the results of Transwell assay also showed that treatment of (+)-Miliusol inhibited the migratory capacity of BT-549 and MDA-MB-231 cells (Fig. S4B). The

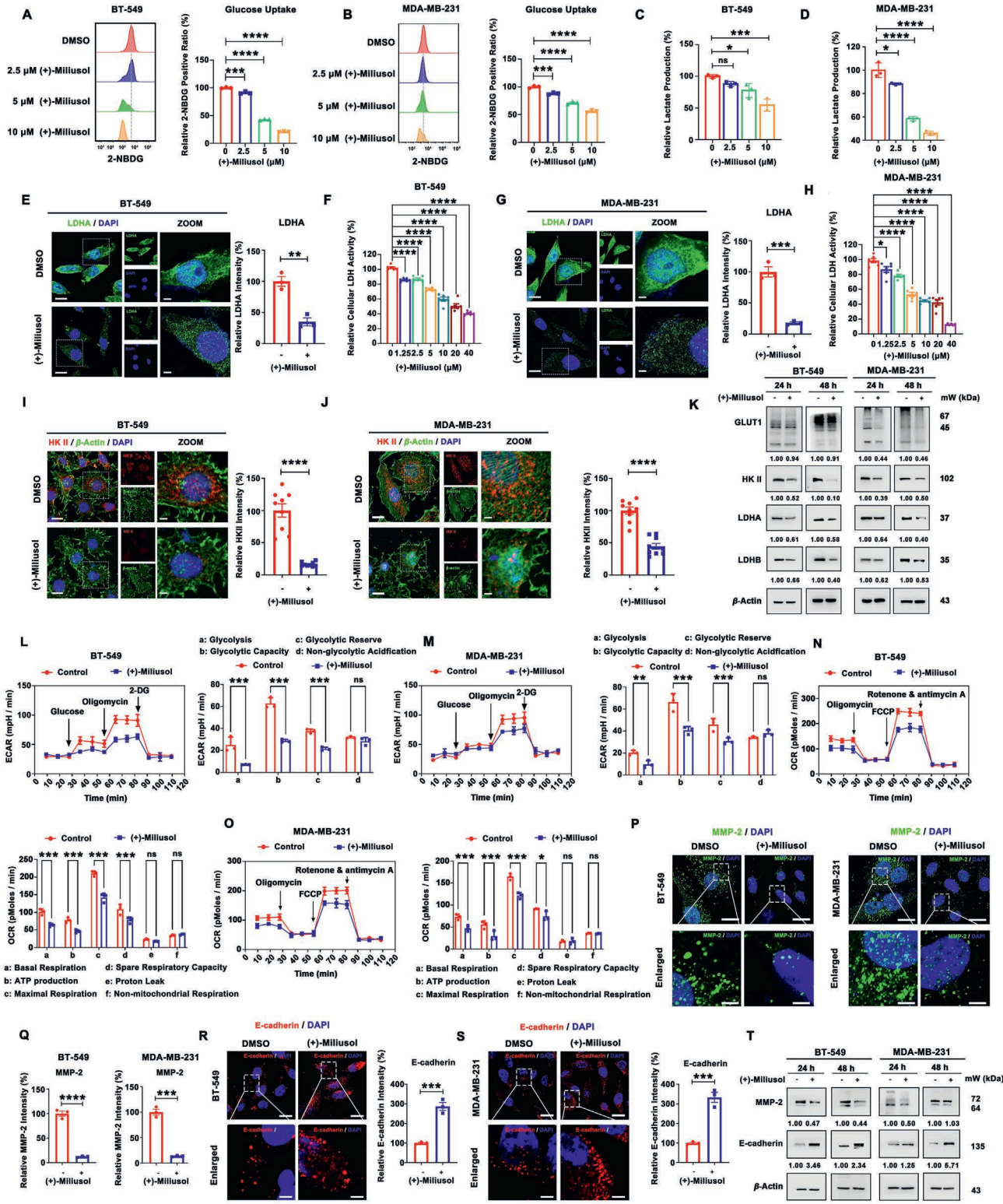

Figure 2 (+)-Miliusol inhibits glycolysis and cell migration in TNBC. (A, B) (+)-Miliusol inhibits the glucose uptake in BT-549 cells and MDA-MB-231 cells. BT-549 cells and MDA-MB-231 cells were treated with 0, 2.5, 5, and 10 μmol/L (+)-miliusol for 24 h, and the glucose uptake ratio was detected by 2-NBDG uptake through flow cytometry. (C, D) BT-549 cells and MDA-MB-231 cells were treated with 0, 2.5, 5, and 10 μmol/L (+)-miliusol for 24 h and the lactic acid production was detected by lactic acid production detection kit. (E, G) Immunofluorescence detection of the expression of LDHA after 5 μmol/L (+)-miliusol treatment. Scale bar = 10 μm. ZOOM Scale bar = 5 μm. The fluorescence intensity of LDHA was calculated using Image J software. (F, H) BT-549 cells and MDA-MB-231 cells were treated with 0, 1.25, 2.5, 5, 10, 20, and 40 μmol/L (+)-miliusol for 24 h and the LDH activity was detected by lactate dehydrogenase activity detection kit. (I, J) Immunofluorescence detection of the expression of HK II after 5 μmol/L (+)-miliusol treatment. Scale bar = 10 μm. ZOOM Scale bar = 5 μm.

expression levels of several key metastasis markers were also evaluated by immunofluorescence staining, including MMP-2[32] and E-cadherin[33]. Remarkably, (+)-miliusol treatment resulted in a significant decrease in MMP-2 intensity, as well as an increase in E-cadherin intensity (Fig. 2P−S), suggesting the impairment of TNBC migration capacity. Furthermore, the immunoblotting results for MMP-2 and E-cadherin confirmed that treatment with (+)-miliusol resulted in the downregulation of MMP-2 and the upregulation of E-cadherin (Fig. 2T, Fig. S3E and S3F), further demonstrating that (+)-miliusol hinders the migration potential of TNBC cells. Taken together, (+)-miliusol attenuated the glycolysis process and migration capacity in TNBC cells.

Interestingly, we conducted a preliminary comparison of the efficacy of (+)-miliusol and a well-established glycolysis inhibitor, 3-bromopyruvic acid (3-BP) [34], which is an inhibitor of the key glycolytic enzyme Hexokinase II. We systematically assessed the differences between 3-BP and (+)-miliusol with respect to cell proliferation, cell migration, and glucose uptake. The findings revealed that (+)-miliusol possesses significantly stronger anti-proliferative, anti-migratory, and anti-glycolytic properties (Supporting Information Fig. S5). These results further substantiate the potential of (+)-miliusol as a novel Warburg effect inhibitor in the treatment of TNBC.

3.3. RNA-seq analysis revealed that ATAD2 and PAK1 are key regulators in (+)-miliusol-induced TNBC cell death

To elucidate the underlying mechanism of the suppressive effects of (+)-miliusol on TNBC cell proliferation and migration, especially its inhibitory functions on the Warburg effect in TNBC cells, we conducted RNA-seq analysis to evaluate the alterations in gene expression upon (+)-miliusol treatment. In BT-549 cells, a total of 4450 genes exhibited significant differential expressions between the control and (+)-miliusol-treated group, among which, 1384 were up-regulated and 3066 were down-regulated (FDR <0.05, and FC > 1.2 or FC < 0.8) (Fig. 3A). In (+)-miliusol-treated MDA-MB-231 cells, 5763 genes exhibited significant differential expressions, and among these, 2827 were up-regulated and 2936 were down-regulated (Fig. 3C). The GO enrichment analysis revealed significant alterations in a panel of key pathways including glycolysis, oxidation-reduction reactions, cell migration, hypoxia response, IRE1-mediated unfolded protein response, MAPK signaling pathway, ERK1/2 activity and autophagy in (+)-miliusol-treated BT-549 cells (Fig. 3B). Similarly, in (+)-miliusol-treated MDA-MB-231 cells, the significantly enriched biological processes included DNA damage, apoptosis, mitochondrial respiratory chain complex I assembly, cell migration, PERK-mediated unfolded protein response, glycolytic process, autophagy, and MAPK signaling (Fig. 3D). The heatmaps show the list of the top 40 significantly altered genes in (+)-miliusol treated BT-549 and MDA-MB-231 cells (Supporting Information Fig. S6A and S6B). Intriguingly, a total of 1957 genes exhibited significant expression alterations in both BT-549 and MDA-MB-231 cell lines as shown by Venn diagram (Fig. 3E). Further GO biological process enrichment analysis demonstrated that these 1957 genes are significantly enriched in tricarboxylic acid cycle (TCA cycle), apoptosis, protein processing in the endoplasmic reticulum, glycolysis, FOXO signaling, mTOR signaling, HIF-1 signaling, MAPK signaling, autophagy, and PI3K−AKT signaling pathways (Fig. 3F). Among these altered pathways and differentially expressed genes, two candidates, *PAK1* and *ATAD2*, were further investigated because of their significant expression changes upon the treatment with (+)-miliusol in both BT-549 and MDA-MB-231 cells. PAK1, a well-conserved serine/threonine protein kinase. Accumulating evidence revealed the upregulated expression pattern of PAK1 in multiple types of cancer, and its functional roles in tumor gene transcription, cell proliferation, migration, apoptosis, and cytoskeleton remodeling[35]. *ATAD2* encodes ATAD2 protein, a member of the AAA ATPase family, which exerts functions on cell proliferation, apoptosis, and metastasis in cancer development and progression through chromatin binding[36]. We constructed a PPI network centered on PAK1 and ATAD2, revealing their regulatory influence on proteins involved in diverse biological processes such as tumor glycolysis, proliferation, metastasis, apoptosis, autophagy, and ER stress (Supporting Information Fig. S6C, Fig. S7A). Next, the mRNA expression levels of *PAK1* and *ATAD2* in both normal and breast cancer tissues were analyzed using GEPIA (http://gepia.cancer-pku.cn/) (Fig. S7B and S7C). The results suggested that the mRNA expression levels of PAK1 and ATAD2 in breast tumor tissues were significantly higher than those in normal breast tissues (ATAD2: Tumor 16.43; Normal 3.42; PAK1: Tumor 37.31; Normal 19.22). We then analyzed the expression levels of PAK1 and ATAD2 in breast cancer patients (https://www.betastasis.com/), and the findings demonstrated elevated expression levels of PAK1 and ATAD2 in breast cancer compared to the normal levels (Fig. S7D and S7E), suggesting that PAK1 and ATAD2 might play functional roles in the carcinogenesis and development of breast cancer. Besides, we also identified and extracted the PAK1- and ATAD2-regulated sub-networks, wherein PAK1 encompassed glycolysis, apoptosis, autophagy and ER stress sub-network (Fig. 3G), while ATAD2 comprised cell metabolism, apoptosis, cell proliferation, and ER stress sub-network (Fig. 3H). Based on these results, we hypothesized that PAK1 might regulate the PI3K−AKT−mTOR pathway and that ERK1/2 activation plays a significant role in TNBC progression. Additionally, ATAD2-mediated activation of c-MYC may also contribute to the metabolic reprogramming of TNBC.

The fluorescence intensity of HKII was calculated using Image J software. (K) Western blot analysis of HK II, GLUT1, LDHA and LDHB protein expression in BT-549 and MDA-MB-231 cells treated 5 μmol/L (+)-miliusol for 24 and 48 h, respectively. β-Actin, loading control. (L, M) The extracellular acidification rate (ECAR) of BT-549 and MDA-MB-231 cells following 24-h treatment with (+)-miliusol was quantified using the Seahorse XF Analyzer. (N, O) The oxygen consumption rate (OCR) of BT-549 and MDA-MB-231 cells following 24-h treatment with (+)-miliusol was measured using the Seahorse XF Analyzer. (P, Q) Immunofluorescence detection of MMP-2 in BT-549 and MDA-MB-231 cells after 5 μmol/L (+)-miliusol treatment. Scale bar = 10 μm. Enlarged Scale bar = 2 μm. The fluorescence intensity of MMP-2 was calculated using Image J software. (R, S) Immunofluorescence detection of E-cadherin in BT-549 and MDA-MB-231 cells after 5 μmol/L (+)-miliusol treatment. Scale bar = 10 μm. Enlarged Scale bar = 2 μm. The fluorescence intensity of E-cadherin was calculated using Image J software. (T) Western blot analysis of MMP-2 and E-cadherin protein expression in BT-549 and MDA-MB-231 cells treated with 5 μmol/L (+)-miliusol for 24 and 48 h, respectively. β-Actin, loading control. Data are presented as mean ± SEM, $n = 3$. ns, no significance; $^{*}P < 0.05$; $^{**}P < 0.01$; $^{***}P < 0.001$; $^{****}P < 0.0001$, compared with the DMSO treated group. M, mol/L.

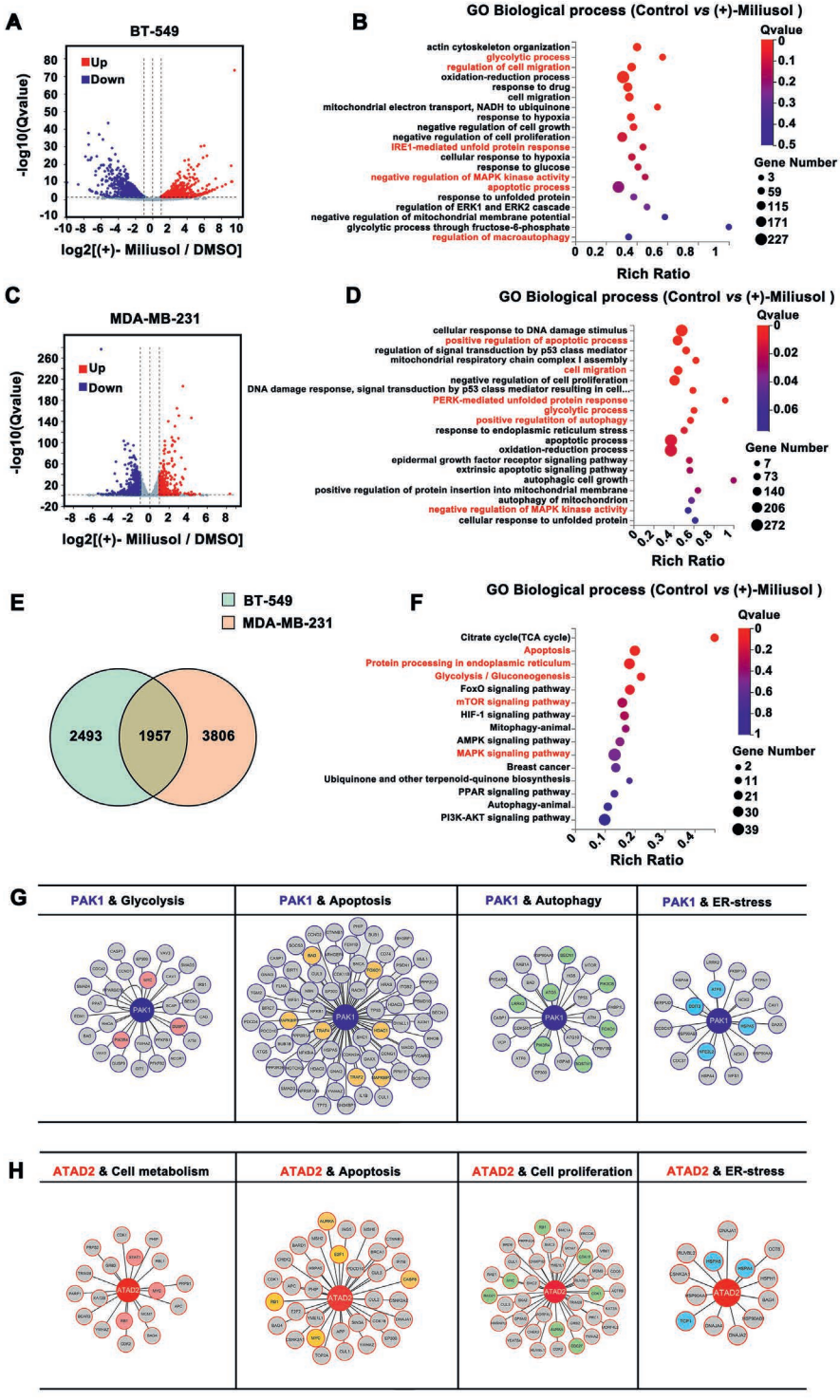

Figure 3 RNAseq analysis of (+)-miliusol treated BT-549 and MDA-MB-231 cells. BT-549 and MDA-MB-231 cells were treated with 5 μmol/L (+)-miliusol for 24 h. (A, C) Volcano plot illustrating the differential expression of genes in BT-549 and MDA-MB-231 cells, with or without (+)-miliusol treatment. The red plots indicate up-regulated genes ($P < 0.05$ and fold change (FC) > 1.2), while the blue plots represent down-regulated genes ($P < 0.05$ and fold change <0.8). (B, D) Bubble plot of pathways enriched by the differentially expressed genes. (E) Overlapping of the genes in (+)-miliusol treated BT-549 and MDA-MB-231 cells. (F) Bubble plot of pathways enriched by the differentially expressed genes in both BT-549 and MDA-MB-231 cells after (+)-miliusol treatment. (G) Extraction of PAK1-centered glycolysis, apoptosis, autophagy and ER stress sub-network. (H) Extraction of ATAD2-centered cell metabolism, apoptosis, cell proliferation and ER stress sub-network.

3.4. (+)-Miliusol blocks ATAD2 and PAK1 regulated Warburg PPI to induce autophagy-related cell death

To validate our hypotheses, the expression levels of ATAD2 and PAK1 in BT-549 and MDA-MB-231 cells upon (+)-miliusol treatment were evaluated. Consistently with their mRNA expression patterns evidenced by RNA-seq analysis, the protein expressions of both ATAD2 and PAK1 significantly decreased upon treatment with (+)-miliusol in TNBC cells by immunofluorescence staining analysis (Fig. 4A−D). Results of immunoblotting also verified the decreased expressions of ATAD2 and PAK1. Further evaluation also demonstrated the decreased phosphorylation status of PAK1, as well as the decreased expression level of the ATAD2 substrate c-MYC after (+)-miliusol treatment. The results indicated that (+)-miliusol significantly inhibited the expression and phosphorylation of PAK1 (Fig. 4E). Similarly, (+)-miliusol demonstrated a potent inhibition of ATAD2 expression and activation, resulting in decreased levels of both ATAD2 and c-MYC (Fig. 4E, Supporting Information Fig. S8A and S8B). Next, the expression of *PAK1* and *ATAD2* was respectively knocked down to further investigate their roles in the tumor suppressive effect of (+)-miliusol. Knockdown of either *PAK1* or *ATAD2* individually resulted in reduced cell viability in TNBC cells; however, even with the absence of PAK1 or ATAD2 individually, (+)-miliusol still exhibited significant inhibition on TNBC cell viability. However, when *ATAD2* and *PAK1* were simultaneously knocked down, the anti-proliferative effect of (+)-miliusol on TNBC cells at low concentrations was not significantly different from that observed in the control group. Only at higher doses did (+)-miliusol exhibit significant anti-proliferative activity against TNBC cells (Fig. 4F and G). Similarly, Ki-67 staining demonstrated that (+)-miliusol could inhibit the proliferation of TNBC cells when either *PAK1* or *ATAD2* was individually knocked down. However, this inhibitory effect was not significant when both *PAK1* and *ATAD2* were simultaneously knocked down (Fig. 4H). Consistent results were observed in the 3D cell spheroid formation assay, demonstrating that the double knockdown of *PAK1* and *ATAD2* significantly inhibited the anti-proliferative effect of (+)-miliusol (Fig. 4I and J). It is noteworthy that treatment of (+)-miliusol still resulted in a significant inhibition of cell viability and proliferation capacity in either *PAK1*- or *ATAD2*-knockdown TNBC cells, however, the folds of inhibition upon treatment were lower than the negative-control (si-NC) group. These findings indicated that (+)-miliusol might exhibit its inhibitory effects on the proliferation of TNBC by modulating pathways associated with PAK1 and ATAD2.

Given that c-MYC, ERK1/2, and AKT pathways are important regulators of glycolysis, playing important roles in tumor cell proliferation and metastasis[37−39], we next examined whether these pathways are involved in PAK1- and ATAD2-mediated anti-tumor effects of (+)-miliusol. The immunofluorescence staining and immunoblotting of p-ERK1/2$^{Thr202/Tyr204}$ confirmed the inhibition of ERK1/2-MAPK signaling in (+)-miliusol-treated BT-549 and MDA-MB-231 cells (Fig. 4K−L). As a key upstream protein of ERK1/2-MAPK, c-Raf, can be activated by the phosphorylation at Ser338 by PAK1[40]. Upon (+)-miliusol treatment, the phosphorylation of c-Raf at Ser338 was remarkably downregulated, indicating the inhibition of PAK1 activity by (+)-miliusol in BT-549 and MDA-MB-231 cells. MEK1/2 can be phosphorylated and activated by c-Raf at Ser217/221, and also by PAK1 at Ser298[41,42]. In our study, (+)-miliusol treatment significantly decreased the phosphorylation of MEK1/2 at both Ser217/221 and Ser298, further confirming the inhibition of PAK1 and c-Raf (Fig. 4M, Fig. S8C−S8F). Next, we investigated the effect of (+)-miliusol on AKT−mTOR pathway and found that (+)-miliusol could inhibit the expression of both AKT and mTOR, as well as the phosphorylated protein expression at Ser473 and Ser2448, respectively (Fig. 4M, Fig. S8C−S8F).

Interestingly, mTOR functions as a critical regulator in both cell proliferation and the complex process of autophagy[43]. Hence, we further examined the expression and phosphorylation of mTOR-regulated downstream autophagy core initiator ULK1 and ULK1 complex proteins. The results showed that (+)-miliusol could effectively activate ULK1 and ULK1 complexes, as evidenced by a significant increase in phosphorylation at Ser555 of ULK1, suppression of phosphorylation at Ser757 of ULK1, and increased phosphorylation levels of mATG13 at Ser355 (Fig. 4N, Fig. S8G−S8J). Notably, the RNA-seq results also indicated a significant induction of autophagy by (+)-miliusol treatment, thereby suggesting the potential of (+)-miliusol treatment to induce autophagy-associated cell death in TNBC cells. Interestingly, we used proteasome inhibitor MG-132 to investigate the effect of protein degradation on protein levels, and it was found that MG-132 was unable to rescue the reduced levels of PAK1, AKT, and other proteins caused by (+)-miliusol, indicating that (+)-miliusol inhibits their expression at the transcriptional or translational level (Supporting Information Fig. S9).

Collectively, our findings confirmed that (+)-miliusol could induce TNBC cell death by inhibiting ATAD2-and PAK1-mediated c-MYC, ERK1/2−MAPK, and AKT−mTOR signaling pathways.

3.5. (+)-Miliusol induces autophagy-related cell death in TNBC cells

Given the intricate interplay between aerobic glycolysis and autophagy in cancer progression[31,44,45], we subsequently investigated the impact of (+)-miliusol on autophagy in BT-549 and MDA-MB-231 cells. Firstly, we labeled the autophagosome marker LC3 (green) and lysosome marker LAMP2 (red) by immunofluorescence. A significant upregulation, accumulation and co-localization of LC3 and LAMP2 puncta were observed upon (+)-miliusol treatment (Fig. 5A and B). In addition, we employed Bafilomycin A1 (Baf. A1, vacuolar H^+-ATPase inhibitor), an autophagy inhibitor, to monitor the autophagy flux. Importantly, the enhanced accumulation and co-localization of LC3 and LAMP2 puncta in (+)-miliusol + Baf. A1-treated group confirmed that (+)-Miliusol-induced autophagy was a continuous process (Fig. 5A and B). Next, BT-549 and MDA-MB-231 cells were transfected with GFP-mRFP-LC3 plasmid and then examined the GFP and RFP fluorescence intensity after treatment with different doses of (+)-miliusol. Consistently, (+)-miliusol induced a dose-dependent increase in the fluorescence intensity of GFP and RFP (Fig. 5C and D). Moreover, we evaluated the expression of key autophagy markers, Beclin-1, SQSTM1/p62 and LC3, and found that (+)-miliusol attenuated the expression of autophagy substrate SQSTM1/p62, and triggered the expression of pro-autophagy regulators Beclin-1 and LC3 (Fig. 5E, Supporting Information Fig. S10). Intriguingly, we observed significant activation of the AMPK pathway in the RNA-seq results. AMPK, an upstream protein of mTOR, can activate ULK1 to induce autophagy. Additionally, AMPK is a well-known energy sensor activated under energy-deficient conditions. Our findings revealed that (+)-miliusol markedly activates AMPK. However, when AMPK

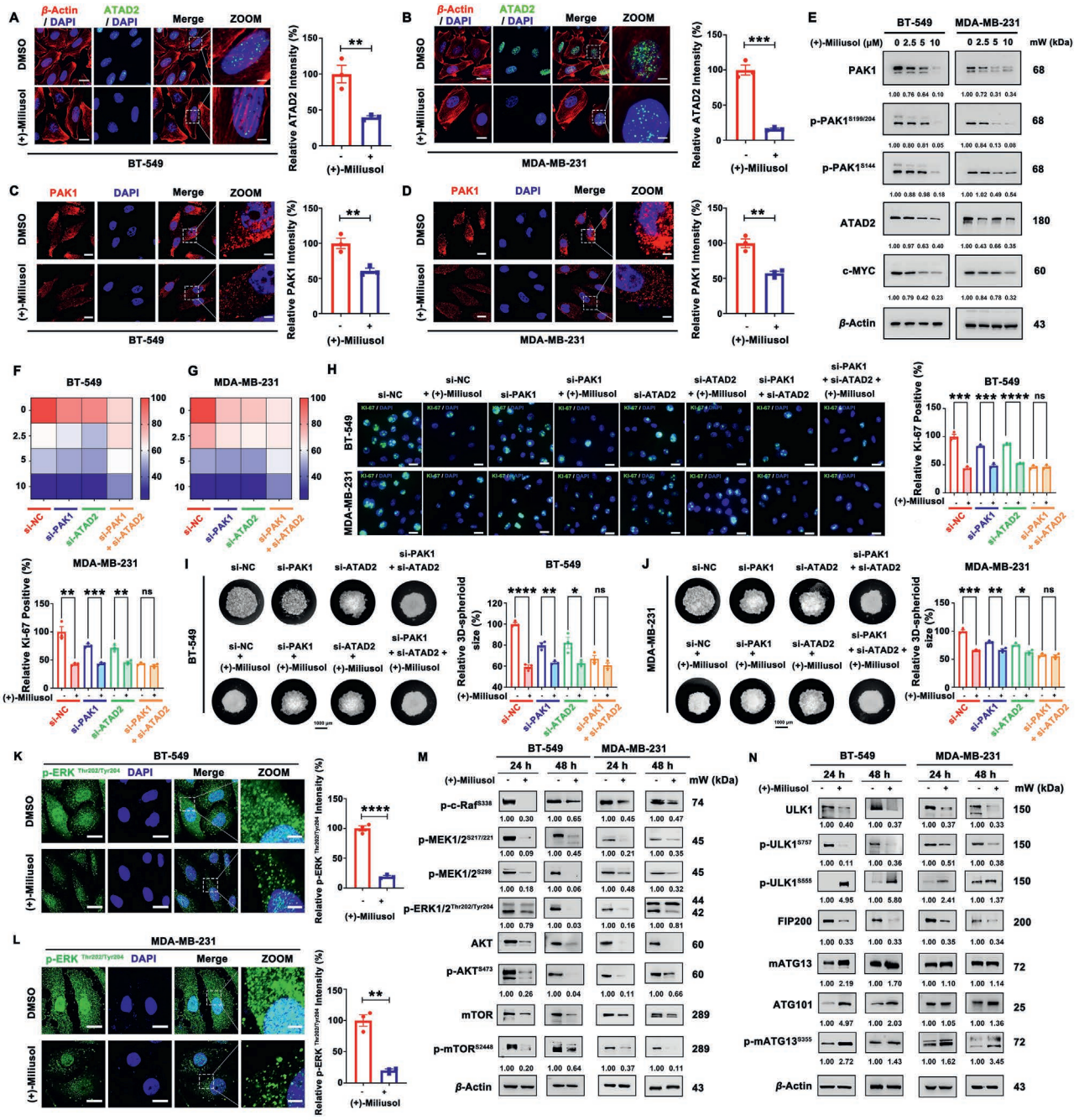

Figure 4 (+)-Miliusol inactivates ATAD2 and PAK1 to regulate BT-549 and MDA-MB-231 cell death. (A, B) Immunofluorescence detection of ATAD2 in BT-549 and MDA-MB-231 cells after 5 μmol/L (+)-miliusol treatment. Scale bar = 10 μm. ZOOM Scale bar = 2 μm. The fluorescence intensity of ATAD2 was calculated using Image J software. (C, D) Immunofluorescence detection of PAK1 in BT-549 and MDA-MB-231 cells after 5 μmol/L (+)-miliusol treatment. Scale bar = 10 μm. ZOOM Scale bar = 2 μm. The fluorescence intensity of PAK1 was calculated using Image J software. (E) Western blot analysis of PAK1, p-PAK1$^{S199/204}$, p-PAK1^{S144}, ATAD2 and c-MYC protein expression in BT-549 and MDA-MB-231 cells treated 0, 2.5, 5, 10 μmol/L (+)-miliusol for 24 h. β-Actin, loading control. (F, G) BT-549 and MDA-MB-231 cells were transfected with si-NC, si-PAK1 or si-ATAD2 plasmid for 48 h, and then after co-incubation with 0, 2.5, 5, and 10 μmol/L (+)-miliusol for another 24 h. (H) Immunofluorescence detection of Ki-67 in BT-549 and MDA-MB-231 cells in different groups. (I, J) Effect of 5 μmol/L (+)-miliusol on 3D-spheroid formation in BT-549 and MDA-MB-231 cells. (K, L) Immunofluorescence detection of p-ERK1/2$^{Thr202/Tyr204}$ in BT-549 and MDA-MB-231 cells after 5 μmol/L (+)-miliusol treatment. Scale bar = 10 μm. ZOOM Scale bar = 2 μm. The fluorescence intensity of p-ERK1/2$^{Thr202/Tyr204}$ was calculated using Image J software. (M) Western blot analysis of p-c-Raf^{S338}, p-MEK1/2$^{S217/221}$, p-MEK1/2^{S298}, p-ERK1/2$^{Thr202/Tyr204}$, AKT, p-AKT^{S473}, mTOR, and p-mTOR^{S2448} protein expression in BT-549 and MDA-MB-231 cells treated 5 μmol/L (+)-miliusol for 24 or 48 h, respectively. β-Actin, loading control. (N) Western blot analysis of ULK1, p-ULK1^{S757}, p-ULK1^{S555}, FIP200, mATG13, ATG101 and p-mATG13^{S355} protein expression in BT-549 and MDA-MB-231 cells treated 5 μmol/L (+)-miliusol for 24 or 48 h,

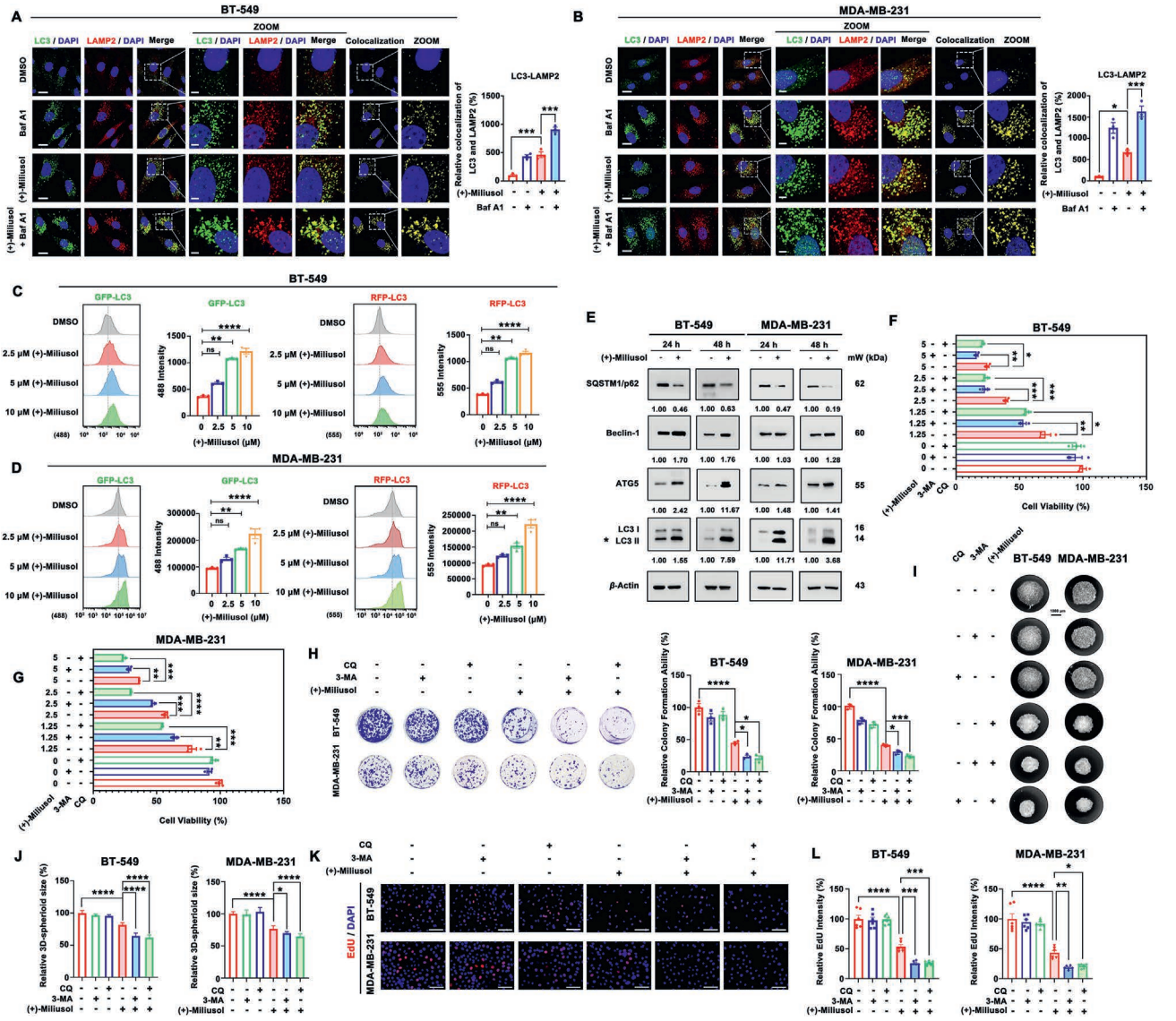

Figure 5 (+)-Miliusol induces autophagy in BT-549 and MDA-MB-231 cells. (A, B) Immunofluorescence detection of LC3 and LAMP2 in BT-549 and MDA-MB-231 cells after 5 μmol/L (+)-miliusol with or without autophagy inhibitor Baf.A1 treatment. Scale bar = 10 μm. ZOOM Scale bar = 2.5 μm. The fluorescence intensity of LC3 and the co-localization of LC3 and LAMP2 were calculated using Image J software. (C, D) BT-549 and MDA-MB-231 cells were transfected with GFP-mRFP-LC3 plasmid for 24 h, and after co-incubation with 2.5, 5, and 10 μmol/L (+)-miliusol for 24 h, the GFP and RFP intensities of the cells were measured by flow cytometry. (E) Western blot analysis of SQSTM1/p62, Beclin-1 and LC3 protein expression in BT-549 and MDA-MB-231 cells treated 5 μmol/L (+)-Miliusol for 24 and 48 h, respectively. *Indicate the statistical strip. (F, G) BT-549 and MDA-MB-231 cells were treated with 0, 1.25, 2.5, and 5 μmol/L (+)-miliusol together with or without autophagy inhibitor 3-MA or CQ for 24 h, respectively. (H) Colony formation assay of BT-549 and MDA-MB-231 cells treated with 5 μmol/L (+)-miliusol together with or without 3-MA or CQ, respectively. (I, J) Effect of 3D-spheroid formation ability of BT-549 and MDA-MB-231 cells treated with 5 μmol/L (+)-miliusol together with or without 3-MA or CQ. (K, L) EdU assay of BT-549 and MDA-MB-231 cells treated with 5 μmol/L (+)-miliusol together with or without 3-MA or CQ, respectively. Scale bar = 100 μm. Data are presented as mean ± SEM, $n = 3$. ns, no significance; *$P < 0.05$; **$P < 0.01$; ***$P < 0.001$; ****$P < 0.0001$. M, mol/L.

was inhibited using its specific inhibitor Compound C[46], the autophagy-promoting effect of (+)-miliusol was substantially diminished (Supporting Information Fig. S11). This demonstrates that AMPK activation plays a crucial role in (+)-miliusol-induced autophagy, potentially triggered by its disruption of energy metabolism in TNBC cells.

Considering the complex role of autophagy in cancer[47,48], we next examined the relationship between autophagy and cell proliferation by employing autophagy inhibitors (3-MA and CQ). Intriguingly, when treated with (+)-miliusol, TNBC cells exhibited significantly lower viability upon inhibition of autophagy as compared to (+)-miliusol treatment alone (Fig. 5F and G,

respectively. β-Actin, loading control. Data are presented as mean ± SEM, $n = 3$. ns, no significance; *$P < 0.05$; **$P < 0.01$; ***$P < 0.001$; ****$P < 0.0001$. M, mol/L.

Supporting Information Fig. S12), suggesting that autophagy induced by (+)-miliusol hindered its anti-proliferative activity. Results of colony formation experiments revealed that inhibition of autophagy could further reduce the colony formation capacity of TNBC cells upon (+)-miliusol treatment (Fig. 5H). Importantly, consistent findings were observed in both the 3D-spheroid formation assay and the EdU proliferation assay (Fig. 5I−L), suggesting that (+)-miliusol-induced autophagy may indeed contribute to the adaptive survival of TNBC cells. This intriguing finding has prompted us to investigate the involvement of autophagy in the mechanisms of (+)-miliusol.

We next investigated whether (+)-miliusol-induced autophagy affected the Warburg effect in BT-549 and MDA-MB-231 cells. The addition of the autophagy inhibitors 3-MA and CQ reduced glucose uptake activity in BT-549 cells and MDA-MB-231 cells (Supporting Information Fig. S13A, S13B, S13D and S13E). Intriguingly, co-treatment with 3-MA and CQ did not significantly affect the lactate production activity in (+)-miliusol-treated BT-549 cells (Fig. S13C). However, the addition of 3-MA significantly decreased the lactate production activity in (+)-miliusol-treated MDA-MB-231 cells; CQ co-treatment also decreased lactate production in (+)-miliusol-treated MDA-MB-231 cells, albeit with no statistically significant difference (Fig. S13F). The expression of key glycolysis regulators, including HK II, LDHA, and LDHB, was subsequently assessed by immunoblotting (Fig. S13K and S13L). The results showed that co-treatment with 3-MA and CQ further enhanced the (+)-miliusol-induced down-regulation of HK II, but exerted different regulatory properties in LDHA and LDHB expression. Co-treatment with 3-MA significantly decreased the expressions of LDHA and LDHB in (+)-miliusol-treated BT-549 cells; however, it exhibited little effects in MDA-MB-231 cells. Co-treatment with CQ significantly decreased LDHA and LDHB expression in both BT-549 cells and MDA-MB-231 cells. The different effects of autophagy inhibitors on LDH expression may account for the observed variations in lactate production activity. These findings confirm that autophagy indeed plays a role in promoting glycolysis in TNBC cells.

In addition, we investigated the effect of (+)-miliusol-induced autophagy on tumor cell migration. Notably, the inhibition of autophagy by 3-MA and CQ did not introduce further inhibition of migration by (+)-miliusol treatment in BT-549 cells. Co-treatment with 3-MA and CQ further enhanced the (+)-miliusol-induced inhibition of migration in MDA-MB-231 cells upon treatment for 48 h, although no significant difference in the folds of inhibition was observed after 24 h treatment (Supporting Information Fig. S14). The results of the Transwell assay further demonstrated that 3-MA significantly influenced the inhibitory effects on cell migration induced by (+)-miliusol treatment in both BT-549 and MDA-MB-231 cells (Fig. S13G−S13J). To confirm these findings, we examined the expression of the migration markers MMP-2 and E-cadherin. Remarkably, co-treatment with (+)-miliusol and 3-MA or CQ enhanced the expression of E-cadherin in both two TNBC cells. However, co-treatment with (+)-miliusol and 3-MA exhibited no further inhibitory effect on the expression of MMP-2 compared to the (+)-miliusol-treated group (Fig. S13M and S13N). It is worth noting that the basal autophagy observed in BT-549 and MDA-MB-231 cells may indicate its cytoprotective function, as evidenced by the significant reduction in glucose uptake activity when these cells were treated solely with 3-MA or CQ. This suggests that dysregulation of basal autophagy might be attributed to the glycolysis-dominated metabolic mode in TNBC cells, which further sustains their metabolic reprogramming.

3.6. EIF3D was discovered and validated as a direct target of (+)-miliusol

Target identification remains a technical challenge for natural active products and is key for elucidating their mechanism of action[49]. To identify the potential direct protein target of (+)-miliusol, we first applied the MS-CETSA technique[22]. Our results revealed a number of potential targets for (+)-miliusol, namely LARS1, SRGAP3, GFPT1, AKR1B15, EIF3D, DDX42 and DOCK7, which emerged as the top seven candidates (Fig. 6A, Supporting Information Fig. S15A). We also used the Western blot (WB)-CETSA experiments to confirm that (+)-miliusol could significantly increase the thermal stability of EIF3D in BT-549 cells and MDA-MB-231 cells, suggesting that (+)-miliusol could directly bind to EIF3D in TNBC cells (Fig. 6B, Fig. S15B and S15C).

To further confirm the direct targeting of EIF3D by (+)-miliusol, we also designed and synthesized a probe Biotin-(+)-Miliusol by biotinylation of (+)-miliusol (Fig. 6C), and biotin-(+)-miliusol showed similar anti-TNBC cell proliferation activity as (+)-miliusol (Fig. S15D). TNBC cells were then co-incubated with Biotin-(+)-miliusol, and the eluent was tested by Western blot (Fig. 6D). The results showed that Biotin-(+)-miliusol could capture EIF3D in a concentration-dependent manner (Fig. 6D, Fig. S15F), further confirming the direct binding of (+)-miliusol to EIF3D. PROTAC is an emerging approach for target protein degradation [50], and has also been applied to target protein identification [51]. Therefore, we further designed and synthesized a PROTAC-(+)-miliusol probe (Fig. 6E), and the PROTAC-(+)-miliusol probe also showed similar anti-TNBC cell proliferation activity as (+)-Miliusol (Fig. S15E). TNBC cells were treated with PROTAC-(+)-miliusol probe for 24 h, followed by the detection of intracellular EIF3D protein levels (Fig. 6F). The results showed that PROTAC-(+)-miliusol can concentration-dependently reduce the protein level of EIF3D in TNBC cells (Fig. 6F, Fig. S15G), further confirming that EIF3D is a direct target of (+)-miliusol. The SPR experiment importantly provided further confirmation that (+)-miliusol could directly bind to EIF3D (K_d = 23.4 μmol/L) (Fig. 6G). Next, the molecular docking revealed that (+)-miliusol occupied the pocket formed by EIF3D, RPS5 and RPS16 subunits. The lactone moiety initiated two key hydrogen bonds with residues Arg418 and Thr469, and an additional hydrogen bond was observed within the unsaturated carbonyl group and Arg418. In addition, the hydroxy group was orientated towards the contact surface of the EIF3D and RPS16 subunits. The geranyl side chain inserted into a hydrophobic pocket formed by EIF3D (residues Asp415, Gly419, Ile422 and Gln470) and RPS5 (Asp37, Lys42, Lys44 and Tyr45). The results suggested that (+)-miliusol could impede the formation of the EIF3D−RPS5−RPS16 complex by binding to EIF3D (Fig. 6H). Next, we examined the effect of (+)-miliusol on the integrity of EIF3D−RPS5−RPS16 complex by protein co-immunoprecipitation. After treatment with (+)-miliusol, the binding of EIF3D to RPS5 and RPS16 was significantly reduced, confirming that (+)-miliusol interfered with the formation of the EIF3D complex (Fig. 6I and J, Fig. S15H and S15I). To further investigate the role of EIF3D in (+)-miliusol induced cell death, we knocked down *EIF3D* and examined the effects of (+)-miliusol on the proliferation and migration potential of TNBC cells. (+)-Miliusol could significantly inhibit the proliferation and migration of TNBC cells, however, following *EIF3D* knockdown, (+)-miliusol did not exhibit a significant effect on the proliferation

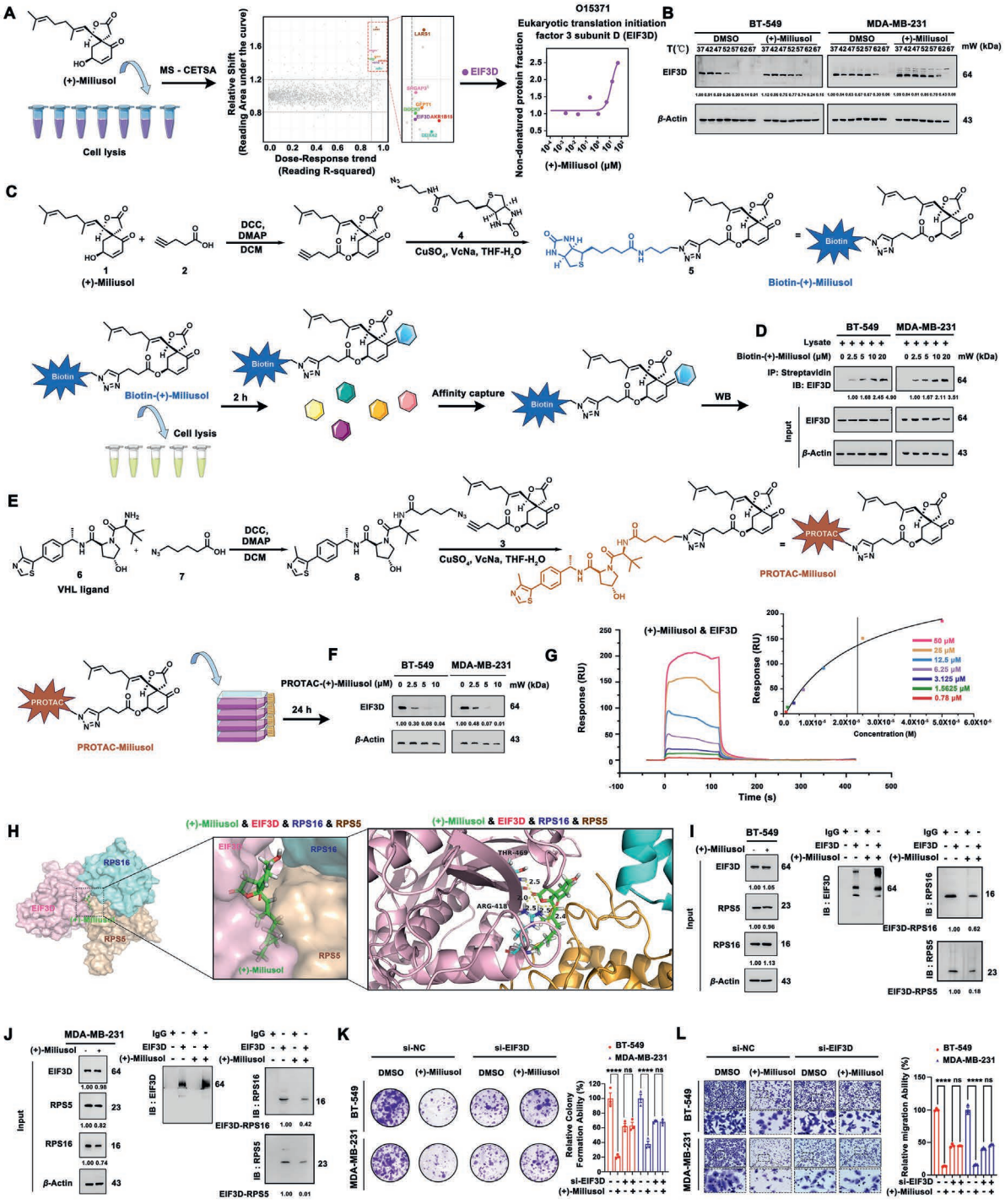

Figure 6 Identification of EIF3D as a target of (+)-miliusol. (A) MS-CETSA result of (+)-miliusol in TNBC cells. (B) WB-CETSA result of BT-549 and MDA-MB-231 cells after treatment with 20 μmol/L (+)-miliusol for 6 h, followed by immunoblotting to detect the expression of EIF3D. (C) The workflow of design and synthesis of biotin-(+)-miliusol probe, and the workflow of biotin-(+)-miliusol for the identification of (+)-miliusol-interacting proteins by *in vitro* pull-down assay in TNBC cells. (D) The pull-down result of BT-549 and MDA-MB-231 cell lysates after incubation with biotin-(+)-miliusol probe for 2 h at room temperature, followed by avidin-agarose beads-mediated pull-down and Western blot experiment. (E) The workflow of design and synthesis of PROTAC-(+)-miliusol. (F) The Western blot results of TNBC cells after treatment with 0, 2.5, 5, and 10 μmol/L PROTAC-(+)-miliusol for 24 h, followed by Western blot detection of the expression of EIF3D. (G) The SPR assay of (+)-miliusol and EIF3D. (H) Molecular docking of (+)-miliusol with EIF3D−RPS5−RPS16 complex. Green: (+)-miliusol; Pink: EIF3D; Blue: RPS16; Brown: RPS5. (I, J) Co-IP results of BT-549 and MDA-MB-231 cells after treatment with 5 μmol/L (+)-miliusol for 24 h, followed by Western blot detection. (K, L) Colony formation assay and transwell assay of (+)-miliusol on si-NC and si-EIF3D transfected TNBC cells. Transwell assay Scale bar = 200 μm. ZOOM Scale bar = 50 μm. Data are presented as mean ± SEM, $n = 3$. ns, no significance; $^{****}P < 0.0001$. M, mol/L.

and migration of TNBC cells when compared to *EIF3D* knockdown alone (Fig. 6K and L), indicating that EIF3D is very important for cell death induced by (+)-miliusol. Taken together, these findings provide robust evidence that EIF3D is a direct target of (+)-miliusol.

3.7. Proteomics analysis revealed that (+)-miliusol suppresses EIF3D-mediated translation of cell survival PPI network

Considering that EIF3D mainly regulates cancer development by controlling protein translation[13,52], we then performed tandem mass tagging (TMT)-based quantitative proteomics to further unravel the mechanisms of (+)-miliusol-induced TNBC cell death. In the (+)-miliusol-treated BT-549 cells sample ($n = 3$), a total of 5394 proteins with at least two peptides were quantified. Using a cutoff of P value ≤ 0.05 and fold change >1.2, we found 1165 proteins up-regulated and 647 proteins down-regulated compared with the control group ($n = 3$), and the top 50 altered proteins ranked by FC and P values were presented in a heatmap (Fig. 7A and C). GO enrichment analysis showed that these differentially expressed proteins were associated with translation, ribosomal subunit, eukaryotic translation initiation factor 3 complex, ribosome, endoplasmic reticulum membrane and rough endoplasmic reticulum membrane (Fig. 7E). Furthermore, KEGG analysis revealed that these proteins are involved in the regulation of some key pathways, including ribosome, glycolysis/gluconeogenesis, cell migration, regulation of TORC1 signaling, protein folding, metabolic pathways and regulation of macroautophagy (Supporting Information Fig. S16A). The PPI network constructed based on the differentially expressed proteins strongly suggests that EIF3D occupies a central position within the network and exerts potentially critical regulatory functions (Fig. S16D).

In the (+)-miliusol-treated MDA-MB-231 cell sample ($n = 3$), a total of 6320 proteins with at least two peptides were quantified. Using a cutoff of P value ≤ 0.05 and FC > 1.2, we found 813 proteins up-regulated and 797 proteins down-regulated compared with the control group ($n = 3$), and the top 50 altered proteins ranked by FC and P values were presented in a heatmap (Fig. 7B and D). GO enrichment analysis showed that these differentially expressed proteins were associated with ribosomal subunit, endoplasmic reticulum membrane, translation, and rough endoplasmic reticulum membrane (Fig. 7F). Furthermore, KEGG analysis revealed that these proteins are involved in the regulation of some key pathways, including glycolysis/gluconeogenesis, apoptotic process, cell migration, autophagy, regulation of TORC1 signaling, protein folding, and response to unfolded protein (Fig. S16B). Similarly, the PPI networks of differentially expressed proteins provide further evidence supporting the crucial role of EIF3D in (+)-miliusol regulation (Fig. S16E). Therefore, we conclude that (+)-miliusol can induce TNBC cell death by regulating EIF3D-mediated translation of key proteins for cellular glycolysis, proliferation, and migration (Fig. S16C).

Consistently with the RNA-seq findings, the proteomic analysis also revealed that (+)-miliusol significantly modulated the PPI network associated with autophagy, metastasis, apoptosis, and protein folding in TNBC cells. Furthermore, PPI networks associated with protein translation showed the most significant changes (Fig. S16F). Since (+)-miliusol may affect mitochondrial function, we next examined the ATP generation capacity of TNBC cells after (+)-miliusol treatment. The results showed that (+)-miliusol significantly decreased ATP production in TNBC cells (Fig. 7G and H), suggesting the disruption of mitochondrial function. In addition, the localization and expression of Snail in TNBC cells were also examined and the results also confirmed that (+)-miliusol could significantly inhibit the protein expression of Snail and its nuclear localization (Fig. 7I and J), suggesting the inhibition of migration. Next, we knocked down *EIF3D* to further confirm its role in (+)-miliusol-regulated TNBC glycolysis and metastasis. Upon *EIF3D* knockdown, TNBC cells exhibited a significant reduction in lactate production. When treated with (+)-miliusol, no additional decrease in lactate generation was observed in TNBC cells (Fig. 7K), indicating that (+)-miliusol primarily depends on modulating EIF3D to regulate glycolysis. By Western blot detection, we found that (+)-miliusol had little effect on the expression level of EIF3D, but could significantly inhibit the expression of its known translation substrate c-Jun[53] (Fig. 7L, Fig. S16G), further confirming the inhibition of (+)-miliusol on the function of EIF3D.

According to the omics results, RUVBL1 is also one of the significantly altered protein after the treatment with (+)-miliusol in TNBC cells, and it has been reported to be closely and positively associated with cancer development[54]. Moreover, RUVBL1 could promote tumor metastasis by activating the β-catenin signaling[55]. Interestingly, RUVBL1 was also found to be up-regulated by EIF3D[56]. By Western blot, we found that (+)-miliusol could significantly inhibit the expression of RUVBL1, β-catenin and the downstream metastasis marker Snail (Fig. 7L). When *EIF3D* was knocked down, (+)-miliusol could no longer further inhibit the expression of β-catenin and snail, confirming that (+)-miliusol mainly relies on EIF3D to suppress TNBC metastasis (Fig. 7M, Fig. S16H and S16I). In addition, the N^6-methyladenosine (m6A) demethylase ALKBH5 plays a crucial role in the regulation of various cellular processes[57] and shows strong associations with various human malignancies, including TNBC[58]. Interestingly, ALKBH5 also contributes to cell glycolysis by facilitating GLUT4 translation[59] and regulate HIF1α. Therefore, we further examined the protein levels of ALKBH5, GLUT4 and HIF1α after (+)-miliusol treatment, and found that (+)-miliusol significantly reduced the expression of ALKBH5, GLUT4 and HIF1α in TNBC cells (Fig. 7N, Fig. S16J and S16K). PKM2 is critical for the Warburg effect. In addition to directly regulating pyruvate to determine the rate of glycolysis[60], PKM2 is also involved in regulating the transcription of genes *(MYC*, *AKT* and *ERK1/2*) related to cancer cell proliferation and migration[61,62]. Our results showed that (+)-miliusol significantly inhibited the protein expression of PKM2, which is consistent with its suppressive effects on glycolysis and metastasis in TNBC cells (Fig. 7N). Upon knockdown of *EIF3D*, (+)-miliusol was no longer able to further suppress the expression of ALKBH5, GLUT4, PKM2, and HIF1α (Fig. 7O, Fig. S16L and S16M), thereby confirming that the inhibitory effect of (+)-miliusol on glycolysis is predominantly mediated through EIF3D. We further examined the impact of (+)-miliusol on the expression levels of PAK1 and ATAD2 following *EIF3D* knockdown. The results demonstrated that after *EIF3D* knockdown, (+)-miliusol was unable to exert additional inhibitory effects on the expression of PAK1 and ATAD2 (Fig. 7O). These findings also corroborate that (+)-miliusol modulates PAK1 and ATAD2 expression through the regulation of EIF3D.

Together, our results suggest that (+)-miliusol can promote TNBC cell death by inhibiting the key proteins involved in EIF3D-mediated cell glycolysis, proliferation, and metastasis.

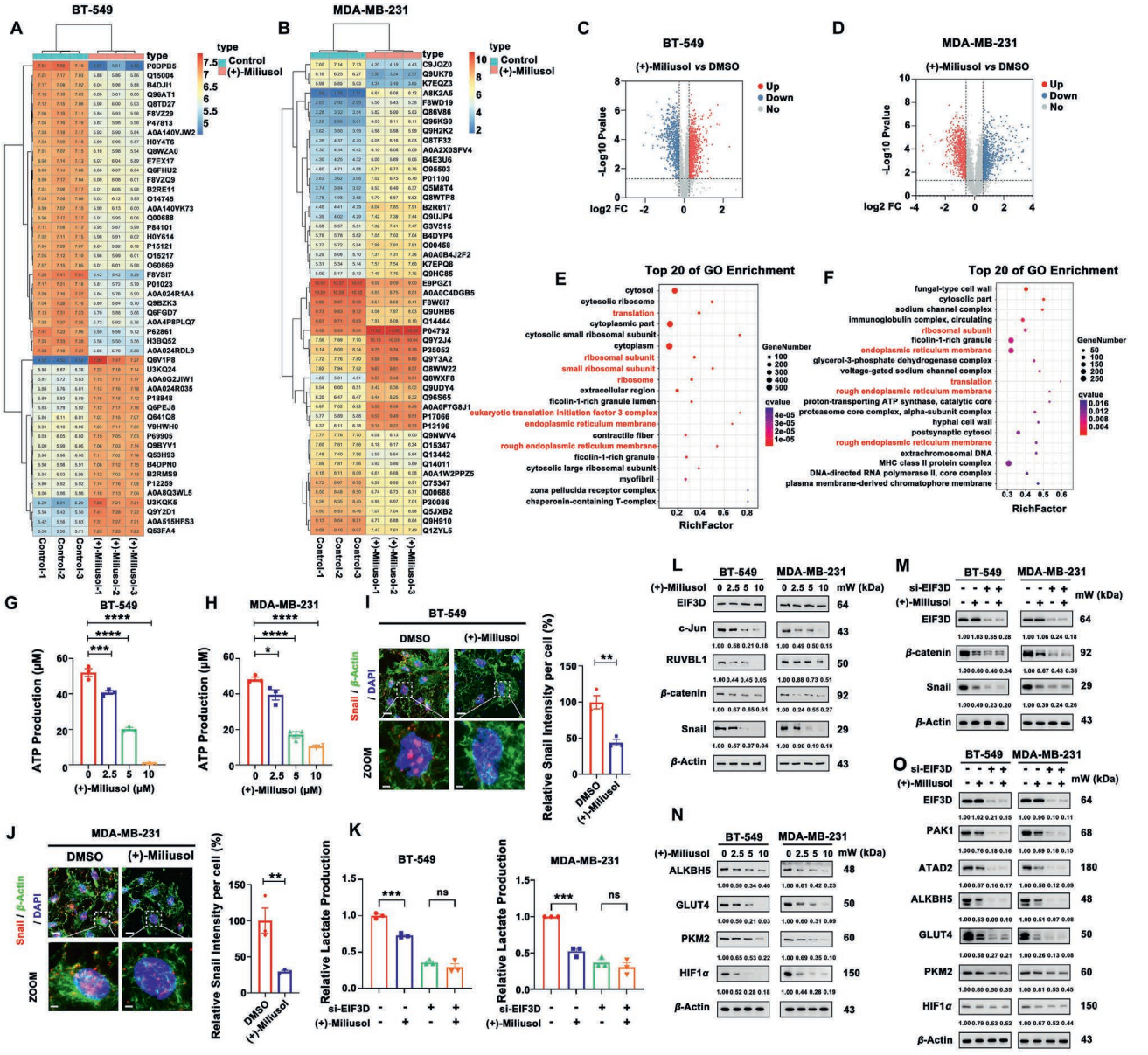

Figure 7 Investigating the mechanism of (+)-miliusol-induced TNBC cell death by proteomics. (A, B) Heatmap of proteins enriched in TNBC cells treated with or without (+)-miliusol, respectively. (C, D) Volcano plot of differentially expressed proteins in TNBC cells treated with or without (+)-miliusol, respectively. (E, F) Top 20 of GO enrichment in BT-549 and MDA-MB-231 cells treated with or without (+)-miliusol, respectively. (G, H) BT-549 and MDA-MB-231 cells were treated with 0, 2.5, 5, and 10 μmol/L (+)-miliusol for 24 h, then measuring the intracellular ATP respectively. (I, J) Immunofluorescence detection of Snail in BT-549 and MDA-MB-231 cells after 5 μmol/L (+)-miliusol treatment. Scale bar = 10 μm. ZOOM Scale bar = 3 μm. The fluorescence intensity of Snail was calculated using Image J software. (K) Detection of lactate content in TNBC cells transfected with si-NC and si-EIF3D after treatment with (+)-miliusol. (L, N) Western blot analysis of EIF3D, c-Jun, RUVBL1, β-catenin, Snail, ALKBH5, GLUT4, PKM2 and HIF1α protein expression in BT-549 and MDA-MB-231 cells treated 0, 2.5, 5, and 10 μmol/L (+)-miliusol for 24 h, respectively. (M, O) Western blot analysis of EIF3D, β-catenin, Snail, PAK1, ATAD2, ALKBH5, GLUT4, PKM2 and HIF1α protein expression in TNBC cells transfected with si-NC and si-EIF3D after treatment with (+)-miliusol. Data are presented as mean ± SEM, $n = 3$. ns, no significance; $^*P < 0.05$; $^{**}P < 0.01$; $^{***}P < 0.001$; $^{****}P < 0.0001$. M, mol/L.

3.8. (+)-Miliusol stimulates ER stress and facilitates apoptosis in TNBC cells

Based on the results of RNA-seq and proteomics analyses, we found that ER stress may be involved in (+)-miliusol-induced cell death. Of note, ER stress is a widely studied cell biological process mainly caused by the accumulation of misfolded proteins in the ER[63]. Recent studies have shown that ER stress is frequently present and has a pivotal role in tumorigenesis, progression, and therapy[64]. EIF3D has also been found to be closely related to ER stress[65]. Transmission electron microscopy was used to observe the submicroscopic structure of TNBC cells treated with 2.5, 5, and 10 μmol/L (+)-miliusol, respectively. It was found that treatment with (+)-miliusol induced significant vacuolation in the cytoplasm of TNBC cells, which was consistent with the characteristics of ER stress (Fig. 8A and B). In addition, with

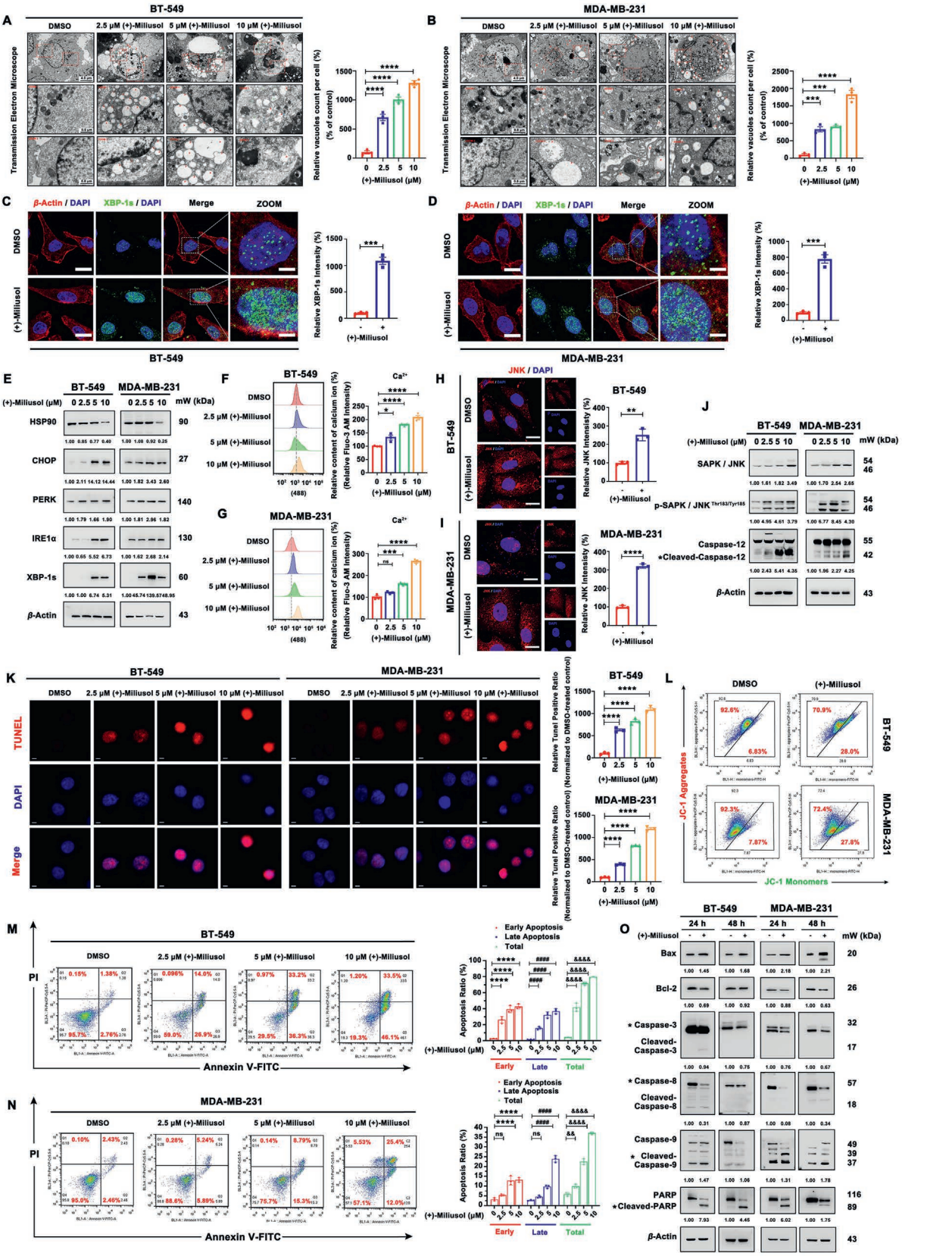

Figure 8 (+)-Miliusol triggers ER Stress and apoptosis in TNBC cells. (A, B) BT-549 and MDA-MB-231 cells were treated with 0, 2.5, 5, and 10 μmol/L (+)-miliusol for 24 h, and then fixed with 2.5% glutaraldehyde. Ultrastructure of cells examined using transmission electron microscopy. Scale bar = 4.0 μm. ZOOM Scale bar = 0.8 μm. Red arrow: intracellular vacuoles; Green arrow: abnormal mitochondria; Blue arrow: autophagosome. (C, D) Immunofluorescence detection of XBP-1s in BT-549 and MDA-MB-231 cells after 5 μmol/L (+)-miliusol treatment.

increasing concentration of (+)-miliusol, the vacuoles gradually became larger, which was accompanied by many abnormal mitochondria and autophagosomes, demonstrating the presence of ER stress and autophagy, as well as the abnormal mitochondrial function induced by the treatment with (+)-miliusol (Fig. 8A and B).

XBP-1s is an important regulator of ER stress, and its activation and nuclear translocation can increase the expression of ER stress-related genes. XBP-1s can also interact with the forkhead box O1 (FoxO1) transcription factor and participate in the regulation of cellular glucose homeostasis[66]. Therefore, we next examined the expression and subcellular localization of XBP-1s by immunofluorescence after 5 μmol/L (+)-miliusol treatment. As shown in Fig. 8C and D, treatment with (+)-miliusol significantly enhanced the expression and nuclear localization of XBP-1s, suggesting a clear activation of XBP-1s induced by (+)-miliusol treatment. We then used immunoblotting to detect some other key regulators of ER stress, including CHOP, PERK, IRE1α, and XBP-1s (Fig. 8E, Supporting Information Fig. S17A and S17B). The expression levels of these positive regulators were increased upon 2.5, 5, and 10 μmol/L (+)-miliusol treatment, further demonstrating that ER stress is involved in (+)-miliusol-induced cell death in TNBC. In addition, HSP90, a protein identified as significantly altered upon (+)-miliusol treatment by proteomics, was also shown to be dose-dependently down-regulated by (+)-miliusol (Fig. 8E). Interestingly, HSP90 is also an emerging anti-tumor target that has been shown to block ER stress by inhibiting IRE1α activity[67]. Inhibition of HSP90 can induce apoptosis of tumor cells [68]. Moreover, both IRE1α and CHOP can induce apoptosis by activating the c-Jun N-terminal kinase JNK, which is involved in various stress processes in cells. Additionally, the ER is an important cellular calcium ion reservoir, and when ER stress occurs, especially severe ER stress, calcium ions in the ER are released into the cytoplasm, causing an imbalance of intracellular calcium ions. Interestingly, severe ER stress can also induce apoptosis by regulating calcium release[69]. Therefore, we determined the level of intracellular calcium ions (Fig. 8F and G), the expression and phosphorylation level of JNK (Fig. 8H and I), and the activation of Caspase-12 (Fig. 8J, Fig. S17C and S17D), a key marker of ER apoptosis, after 2.5, 5, and 10 μmol/L (+)-miliusol treatment in BT-549 and MDA-MB-231 cells. Intriguingly, treatment with (+)-miliusol could increase the intracellular calcium level and promote the activation of JNK and Caspase-12, demonstrating the occurrence of ER stress-induced apoptosis. In addition, the results of TUNEL assay showed that (+)-miliusol induced apoptosis in a dose-dependent manner with remarkable accumulation of DNA breaks (Fig. 8K). In addition, JC-1 staining and Annexin V/PI staining showed that (+)-miliusol induced significant mitochondrial membrane potential reduction and apoptosis (Fig. 8L−N). To investigate the underlying mechanism of (+)-miliusol-induced apoptosis, we next examined the expression of some key apoptosis markers by Western blot analysis. The results demonstrated that treatment with (+)-miliusol elicited activation of the mitochondrial-regulated apoptotic pathway, as evidenced by the upregulation of Bax and down-regulation of Bcl-2 expression, along with enhanced cleavage of Caspase-9, Caspase-3, PARP, and Caspase-8 (Fig. 8O, Fig. S17E−S17H), suggesting that the death receptor-mediated apoptotic pathway might also involve in (+)-miliusol-induced apoptosis.

The impact of autophagy on apoptosis was further examined in our investigation. The results showed that co-treatment with 3-MA and CQ significantly increased the ratio of cells in late apoptosis phase when treated with a high dose of (+)-miliusol in both BT-549 and MDA-MB-231 cells, but had little or less significant effect at a low dose of (+)-miliusol (Supporting Information Fig. S18A−S18D). Co-treatment of (+)-miliusol and 3-MA or CQ further enhanced the cleavage of Caspase-8 in BT-549 and MDA-MB-231 cells. Treatment with 3 MA or CQ significantly increased the levels of Bax and cleaved-caspase-9 following (+)-miliusol treatment. However, no statistically significant difference was observed in cleaved-caspase-9 levels in BT-549 cells, although an upward trend was noted. Regarding PARP, treatment with 3 MA or CQ further decreased overall PARP levels after (+)-miliusol treatment, indicating enhanced apoptosis after autophagy inhibition (Fig. S18E−S18G). It is noteworthy that the inhibition of AMPK significantly enhances the upregulation of Bax by (+)-miliusol, thereby providing further evidence that the suppression of autophagy promotes apoptosis induced by (+)-miliusol (Fig. S11). In summary, (+)-miliusol effectively induces ER stress, which subsequently triggers the release of intracellular calcium ions and ultimately promotes cellular apoptosis. Notably, the autophagy induced by (+)-miliusol partially counteracts its pro-apoptotic effects.

3.9. (+)-Miliusol has a therapeutic potential by modulating EIF3D-regulated cell death in vivo

Considering the promising anti-tumor effect of (+)-miliusol in TNBC cells, we next investigated its anti-tumor potential in TNBC xenograft model. We established nude mouse xenograft models of BT-549 cells and MDA-MB-231 cells. The results showed that treatment with (+)-miliusol also exerted a significant suppressive effect in BT-549 and MDA-MB-231 xenograft growth *in vivo* (Fig. 9A−F). Since autophagy was found to be involved in (+)-miliusol-induced tumor cell death *in vitro*, we also

Scale bar = 10 μm. ZOOM Scale bar = 2.5 μm. The fluorescence intensity of XBP-1s were calculated using Image J software. (E) BT-549 and MDA-MB-231 cells were treated with 0, 2.5, 5, and 10 μmol/L (+)-miliusol for 24 h, and then Western blot analysis of HSP90, CHOP, PERK, IRE1α and XBP-1s protein expression levels. β-Actin, loading control. (F, G) BT-549 and MDA-MB-231 cells were treated with 0, 2.5, 5, and 10 μmol/L (+)-miliusol for 24 h, the content of intracellular calcium ion was then detected by Fluo-3 AM probe. (H, I) Immunofluorescence detection of JNK in BT-549 and MDA-MB-231 cells after 5 μmol/L (+)-miliusol treatment. Scale bar = 10 μm. (J) Western blot analysis of SAPK/JNK, p-SAPK/JNK$^{Thr183/Tyr186}$ and caspase-12 protein expression levels. β-Actin, loading control. *Indicate the statistical strip. (K) TUNEL assay detection of apoptosis of TNBC cells treated with 0, 2.5, 5, and 10 μmol/L (+)-miliusol for 24 h. (L) JC-1 staining of TNBC cells treated with 0, 5 μmol/L (+)-miliusol for 24 h to examine the mitochondrial membrane potential. (M, N) Annexin V-PI staining of TNBC cells treated with 0, 2.5, 5, 10 μmol/L (+)-miliusol for 24 h to examine the apoptosis ratio. (O) Western blot analysis of Bax, Bcl-2, caspase-8, caspase-9, caspase-3 and PARP expression in BT-549 and MDA-MB-231 cells treated 5 μmol/L (+)-miliusol for 24 and 48 h, respectively. β-Actin, loading control. *Indicate the statistical strip. Data are presented as mean ± SEM, $n = 3$. ns, no significance; $^{*}P < 0.05$; $^{**}P < 0.01$; $^{***}P < 0.001$; $^{****}P < 0.0001$, $^{\#}P < 0.05$; $^{\#\#}P < 0.01$; $^{\#\#\#}P < 0.001$; $^{\#\#\#\#}P < 0.0001$, $^{\&}P < 0.05$; $^{\&\&}P < 0.01$; $^{\&\&\&}P < 0.001$; $^{\&\&\&\&}P < 0.0001$. M, mol/L.

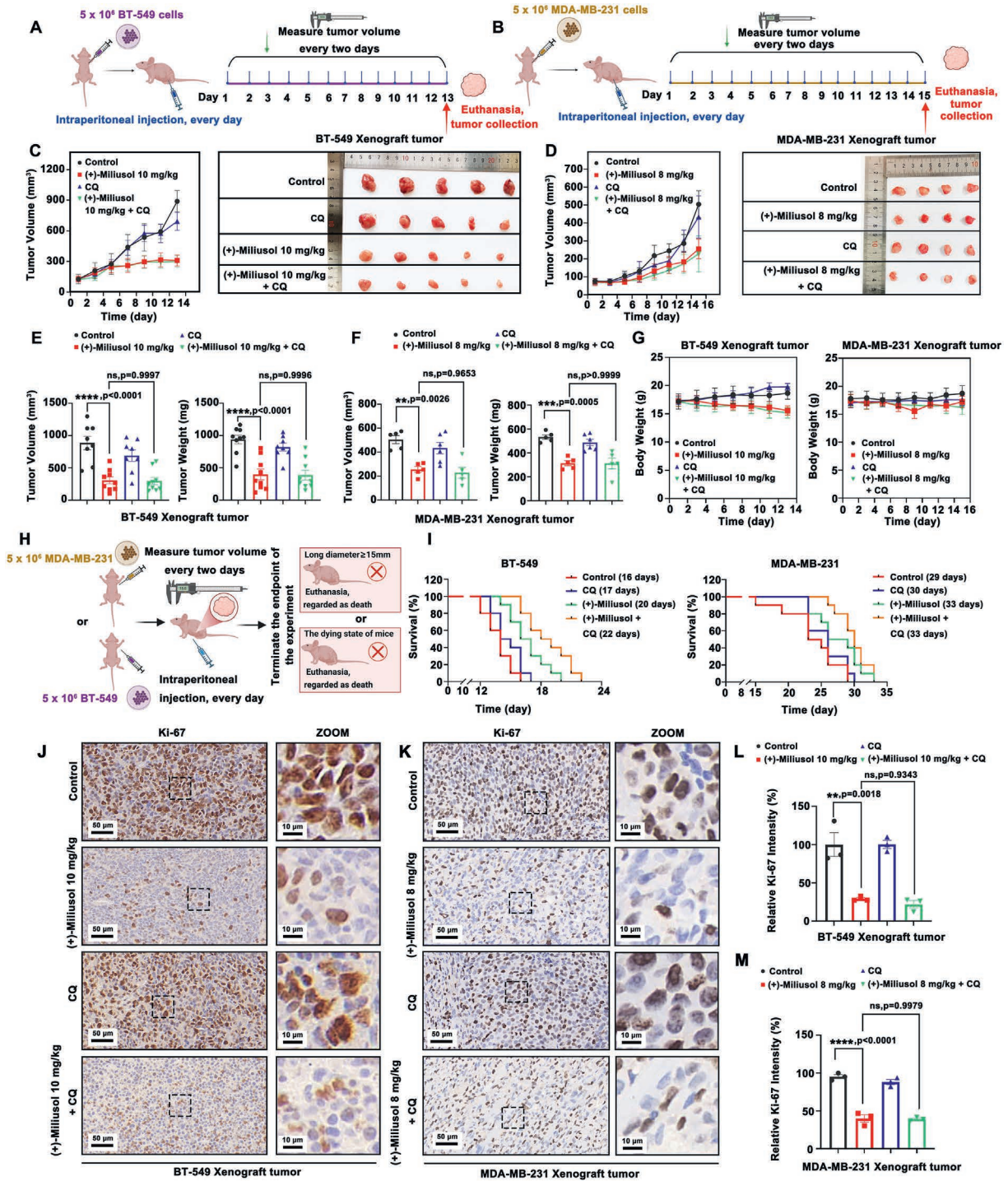

Figure 9 (+)-Miliusol inhibits tumor growth in TNBC xenograft model. (A, B) The experimental protocol for xenografting BT-549 and MDA-MB-231 cells in nude mice. (C, D) Change in tumor volume during drug treatment. MDA-MB-231 and BT-549 tumor-bearing xenograft mice were treated with vehicle control or (+)-miliusol, CQ and (+)-miliusol + CQ treatment once daily. The tumor volume data were collected daily and presented as the mean ± standard error of the mean (SEM). The representative tumor images for each group were obtained on the final day. (E, F) Tumor volume and tumor weight data were collected at the final day and presented as mean ± SEM, $n = 6-8$. (G) Changes in body weight during drug treatment. (H) Experimental protocol for the survival curve of xenograft tumors of nude mouse BT-549 and MDA-MB-231 cells. (I) Survival curve analysis of BT-549 and MDA-MB-231 xenograft tumor models. In the BT-549 xenograft tumor models, the Control group *vs* CQ group, ns, $P = 0.1066$; the Control group *vs* (+)-miliusol group, $^{***}P = 0.0009$; the Control group *vs* (+)-miliusol + CQ group, $^{****}P < 0.0001$; the (+)-miliusol group *vs* (+)-miliusol + CQ group, $^{\#}P = 0.0367$. In the MDA-MB-231 xenograft tumor models, the Control group *vs* CQ group, ns, $P = 0.2638$; the Control group *vs* (+)-miliusol group, $^{*}P = 0.0297$; the Control group *vs* (+)-miliusol + CQ group, $^{***}P = 0.0004$; the (+)-miliusol group *vs* (+)-miliusol + CQ group, ns, $P = 0.2181$. (J–M) Immunohistochemical analysis of proliferation

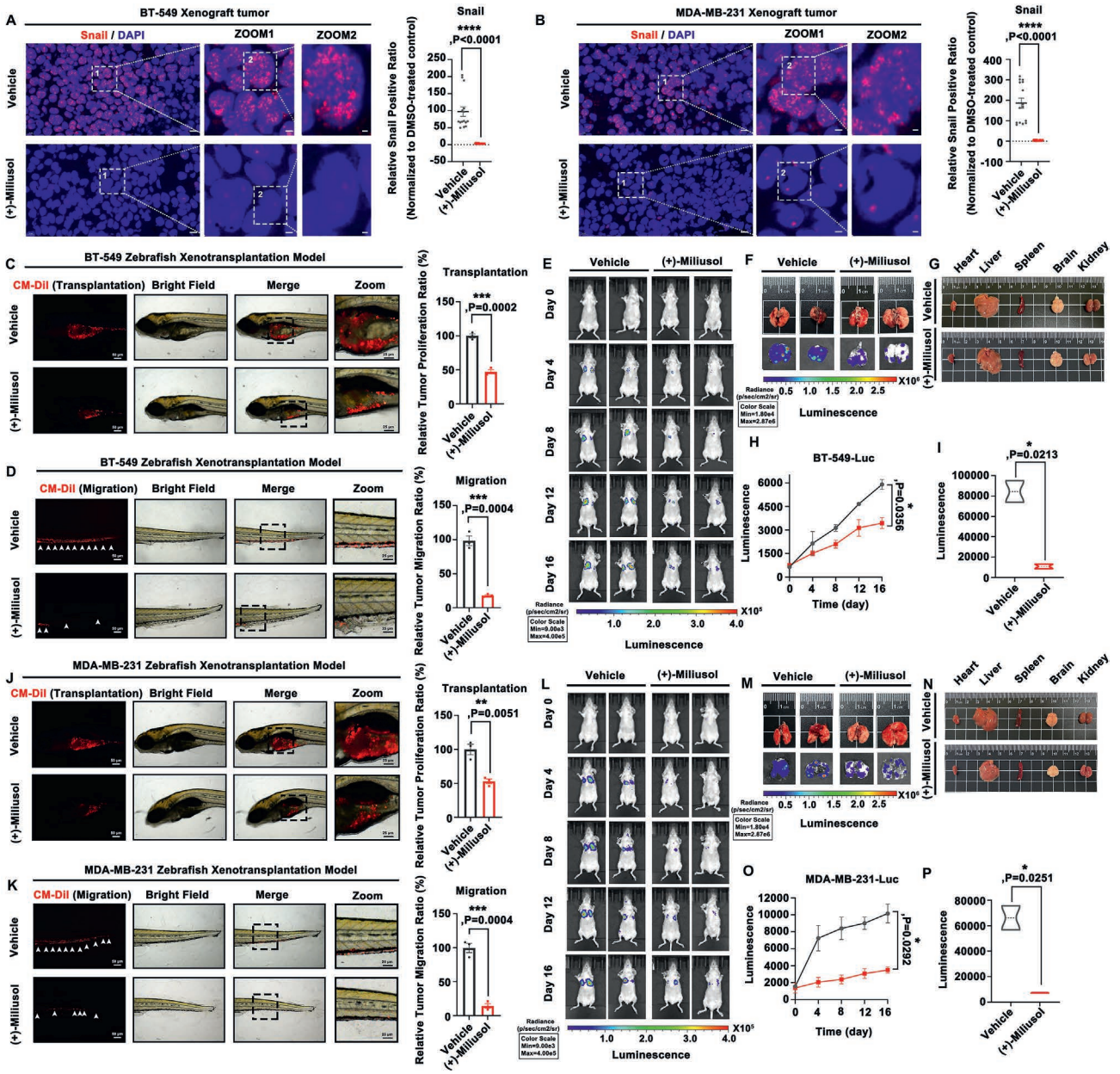

Figure 10 (+)-Miliusol inhibits tumor metastasis in TNBC xenograft models. (A, B) Immunofluorescence detection of Snail levels in tumor tissues of BT-549 cells and MDA-MB-231 cells xenograft mice. Scale bar = 10 μm. ZOOM1 Scale bar = 2.5 μm. ZOOM2 Scale bar = 1 μm. (C, D, J, K) The images illustrate representative immunofluorescence of CM-Dil-labelled BT-549 and MDA-MB-231 cells in xenograft zebra fish. The treatment dosage of (+)-miliusol was 2.0 μg/mL. CM-Dil intensity was measured using ImageJ software. Tumor proliferation and migration ratio were quantified by comparison with the control group. (E, L) Representative images of BT-549-LUC cells and MDA-MB-231-LUC cells metastasis in mice, respectively. (F, M) Representative images of BT-549-LUC cells and MDA-MB-231-LUC cells metastasis in mice lung, respectively. (G, N) The images provided represent the organs of mice, namely the heart, liver, spleen, brain and kidney, respectively. (H, O) TNBC cell metastasis intensity statistics during (+)-miliusol treatment. (I, P) TNBC cell metastasis intensity statistics in lung during (+)-miliusol treatment. Date is presented as mean ± SEM, $n = 3$. ns, no significance; $^{*}P < 0.05$; $^{**}P < 0.01$; $^{**}P < 0.001$; $^{****}P < 0.0001$, compared with the vehicle control group.

investigated whether autophagy inhibition by CQ could affect the *in vivo* anti-tumor potential of (+)-miliusol. The results showed that the autophagy inhibitor CQ did not significantly affect the effect of (+)-miliusol on the tumor proliferation rate, tumor volume, and tumor weight (Fig. 9A−F). We also found that the body weight of the nude mice in the (+)-miliusol and (+)-miliusol + CQ groups gradually decreased with the administration time; this was most notable in the (+)-miliusol group

marker Ki-67. Scale bar = 50 μm. ZOOM Scale bar = 10 μm. Date are presented as mean ± SEM, $n = 3$. ns, no significance; $^{**}P < 0.01$; $^{****}P < 0.0001$, compared with the vehicle control group. M, mol/L.

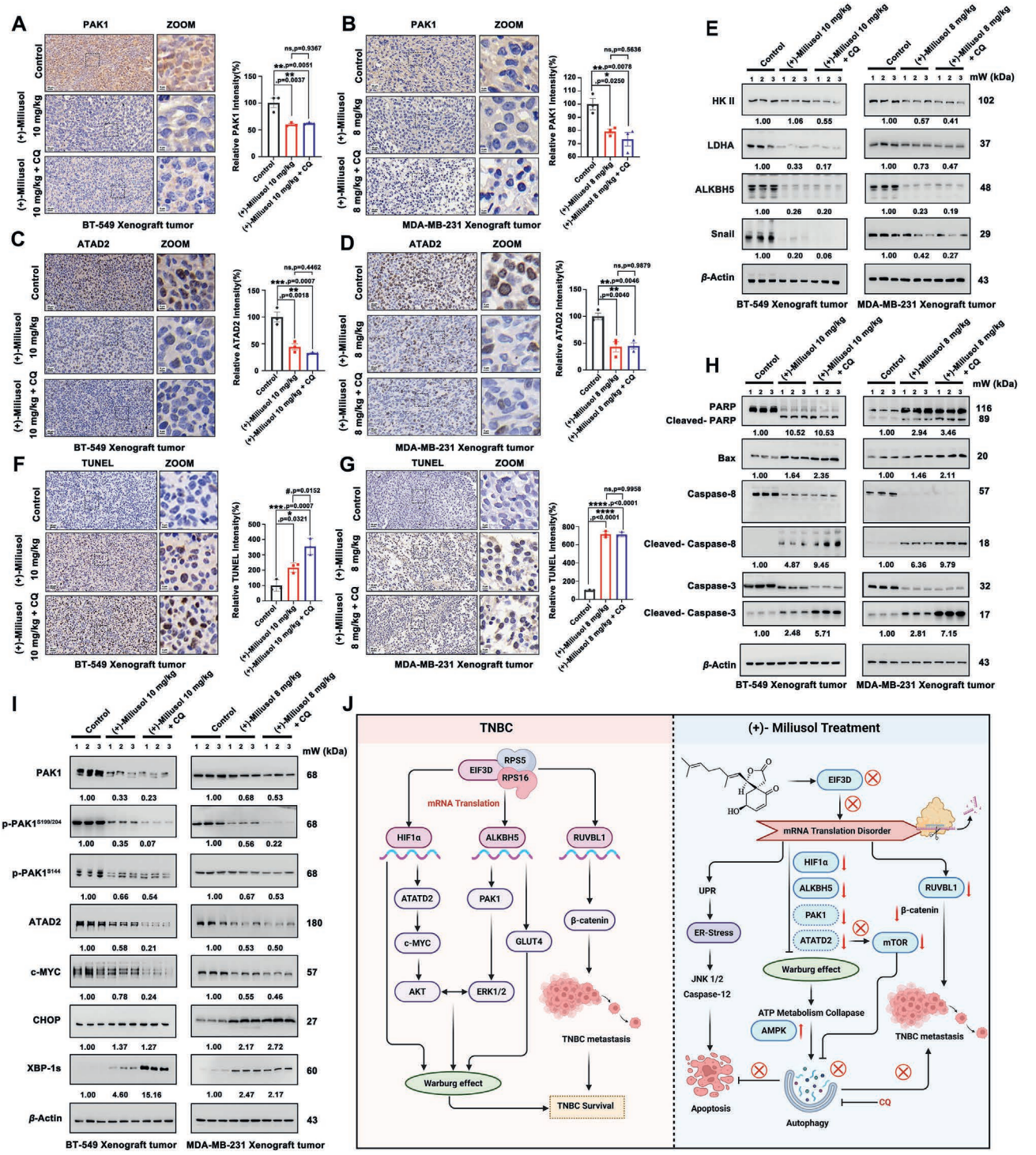

Figure 11 (+)-Miliusol has therapeutic potential in regulating glycolysis, apoptosis, autophagy, migration, and ER-stress *in vivo*. (A−D) Immunohistochemical analysis PAK1 and ATAD2. Scale bar = 20 μm. ZOOM Scale bar = 5 μm. (E) Western blot analysis of HK II, LDHA, ALKBH5 and Snail protein expression levels of tumor tissues in different group. β-Actin, loading control. (F, G) Immunohistochemical analysis of apoptosis marker TUNEL assay. Scale bar = 20 μm. ZOOM Scale bar = 5 μm. (H) Western blot analysis of PARP, Bax, Caspase-8 and Caspase-3 protein expression levels of tumor tissues in different group. β-Actin, loading control. (I) The Western blot analysis was performed to determine the protein expression levels of PAK1, phospho-PAK1$^{S199/204}$, phospho-PAK1^{S144}, ATAD2, c-MYC, CHOP and XBP-1s in different experimental groups. The protein β-actin was utilised as a loading control. (J) The mechanism diagram of (+)-miliusol in TNBC treatment. Date is presented as mean ± SEM, $n = 3$. ns, no significance; $^{*}P < 0.05$, $^{**}P < 0.01$, $^{***}P < 0.001$, $^{****}P < 0.0001$.

(Fig. 9G), which showed a decrease on the 10th day of administration, suggesting that (+)-miliusol might has a slight toxicity. Subsequently, we systematically evaluated the survival rates of each group of mice and generated Kaplan−Meier survival curves. Our results demonstrated that (+)-miliusol significantly improved the survival rate of tumor-bearing mice. Moreover, the combination of CQ and (+)-miliusol exhibited a synergistic effect, further enhancing the survival rate of TNBC xenograft mice, particularly in the BT-549 cell xenograft model (Fig. 9H and I). Importantly, both (+)-miliusol and (+)-miliusol + CQ significantly inhibited tumor proliferation, as demonstrated by Ki-67 staining, although there was no statistically significant difference between the two groups (Fig. 9J−M). These results also indicate that the incorporation of autophagy inhibitors in long-term treatment may potentially provide greater benefits.

To investigate the safety of (+)-miliusol, we first examined its effect on the blood routine of nude mice (Supporting Information Fig. S19A and S20A). The results indicated that no statistically significant differences were observed in the blood routine parameters between the (+)-miliusol treatment group and the control group. In addition, HE staining also showed that the effects of (+)-miliusol treatment on major organs (brain, heart, liver, spleen, lung, kidney, stomach and intestine) in nude mice were not statistically different from those in the control group (Fig. S19 and S20). Considering that general natural anti-tumor drugs have immunosuppressive effects, we preliminarily tested the effect of (+)-miliusol on B cells in the blood and spleen of nude mice. The results showed that (+)-miliusol had no significant effect on the content of B cells (Fig. S19C and S20C). Furthermore, in BALB/c mice, we evaluated the effects of (+)-miliusol on blood parameters, major organs, and T and B lymphocytes in the blood, thymus, and spleen. The results also indicated no significant toxicity throughout the treatment period with (+)-miliusol (Supporting Information Fig. S21). We also examined the survival rates of each group in immune-competent 4T1 tumor-bearing mice, and the results also indicated that CQ could enhance the survival rate of tumor-bearing mice treated with (+)-miliusol (Supporting Information Fig. S22A and S22B). We further investigated the effects of (+)-miliusol on T cell trafficking, activation, and cytotoxicity in immunocompetent mice bearing 4T1 tumors (Fig. S22C−S22J). The results showed that T cells were not significantly activated in either the blood or tumor tissue, indicating that (+)-miliusol does not exert its anti-TNBC effects through T cell activation. In conclusion, (+)-miliusol is relatively safe in mice overall.

Next, we proceeded to examine the impact of (+)-miliusol on the metastatic potential of TNBC *in vivo*. First, we employed immunofluorescence staining to evaluate the expression levels of the migration marker Snail in TNBC tumors. The results demonstrated that Snail was highly expressed in the nucleus of tumor tissues under normal conditions, whereas treatment with (+)-miliusol significantly attenuated Snail expression (Fig. 10A and B). Subsequently, we investigated the impact of (+)-miliusol in a zebrafish heterograft model. (+)-Miliusol demonstrated promising potential as an anti-proliferative and anti-metastatic agent in xenografted zebrafish models of BT-549 and MDA-MB-231 cells (Fig. 10C, D, J, K). We intravenously injected BT-549-LUC and MDA-MB-231-LUC cells into nude mice to evaluate the anti-TNBC metastatic potential of (+)-miliusol. The experimental results demonstrated that treatment with (+)-miliusol significantly suppressed the migration rate of both BT-549-LUC and MDA-MB-231-LUC cells (Fig. 10E, H, L, O). Furthermore, upon sacrificing the mice on day 16, (+)-miliusol exhibited a remarkable reduction in lung metastasis intensity in TNBC cells (Fig. 10F, I, M, P). The presence of TNBC metastasis in other major organs was not significant, and there were no notable differences observed between all organs and the control group (Fig. 10G, N). Consequently, (+)-miliusol exhibited robust potential as an anti-TNBC metastasis agent *in vivo*.

To verify the underlying mechanism of the anti-tumor effect of (+)-miliusol *in vivo*, we assessed the expression and activity of PAK1 and ATAD2 in tumor tissues. Results of both immunochemistry staining and Western blot assay suggested a significant inhibition of PAK1 expression and phosphorylation, as well as a remarkable down-regulation of ATAD2 and its downstream c-MYC, suggesting that (+)-miliusol could inhibit PAK1 and ATAD2 *in vivo* (Fig. 11A−D and I, Supporting Information Fig. S24). We also evaluated the expression of glycolysis markers HK II and LDHA, and migration markers Snail and E-cadherin by Western blot. Results revealed a significant decrease in the expression of both HK II, ALKBH5 and LDHA, indicating that (+)-miliusol significantly inhibited the Warburg effect of tumors *in vivo* (Fig. 11E, Fig. S24). Similarly, after (+)-miliusol treatment, the expression of Snail was significantly downregulated, and that of E-cadherin was significantly upregulated (Fig. 11E, Supporting Information Fig. S23).

Next, we examined the ratio of apoptotic cells in the tumor tissue by TUNEL assay, and the results showed that both (+)-miliusol and (+)-miliusol + CQ treatment induced a significant increase in the apoptotic cell ratio in the tumor tissue, albeit with no statistically significant difference between these two groups (Fig. 11F and G). We also examined the expression of PARP, Bax, Caspase-8, and Caspase-3 by Western blot, and found that both (+)-miliusol and (+)-miliusol + CQ treatment significantly increased the cleavage of PARP, caspase-8, and caspase-3, and enhanced the expression of Bax, suggesting that (+)-miliusol significantly induced cell apoptosis *in vivo*. Interestingly, co-treatment with CQ further enhanced the regulatory functions of (+)-miliusol on the expressions of these proteins (Fig. 11H, Fig. S24), indicating that inhibition of autophagy could promote (+)-miliusol-induced apoptosis, which is consistent with the *in vitro* results. In addition, we found that (+)-miliusol facilitated LC3 expression, while CQ further enhanced the accumulation of LC3 induced by (+)-miliusol (Fig. S23), demonstrating the progression of autophagy. Furthermore, results of Western blot also suggested that (+)-miliusol treatment could up-regulate the expression of ER stress markers, including CHOP and XBP-1s, suggesting that (+)-miliusol could also induce ER stress *in vivo* (Fig. 11I, Fig. S24). Taken together, these findings suggest that (+)-miliusol exhibits considerable therapeutic potential through the inhibition of EIF3D, thereby modulating key biological processes including glycolysis, apoptosis, autophagy, cell migration, and ER stress *in vivo* (Fig. 11J).

4. Discussion

Breast cancer presently ranks second in global incidence among all types of cancers. Among its subtypes, TNBC is the most malignant one with an unfavorable prognosis, characterized by early onset, extensive metastasis, and frequent recurrence[2]. However, due to the lack of a unified and effective therapeutic target, the clinical treatment of TNBC still relies on surgical resection and chemotherapy[70]. Despite the advances in novel therapeutic

strategies against cancers, such as targeted small molecule drugs, biological antibody drugs, and nucleic acid therapy, there remains a dearth of satisfactory outcomes in the treatment of TNBC. The primary factor contributing to this problem is the substantial heterogeneity observed in TNBC, not only among patients but also within tumor tissue from the same patient[4]. As a result, TNBC exhibits relative insensitivity to single-target inhibition, and compensatory signaling pathways associated with drug resistance may emerge shortly after. To date, the most successful case of novel drug development in TNBC is the use of PARP inhibitors (olaparib[71,72] and talazoparib[73]) based on synthetic lethality in *BRCA1/2*-mutated TNBC. However, the emergence of resistance to PARP inhibitors has raised concerns about the future prospects of TNBC treatment. PI3K/AKT inhibitors (capivasertib[74] and ipatasertib[75]) also bring new hope to TNBC treatment, but there is also a serious problem of susceptibility to drug resistance. Research into immune checkpoint inhibitors and antibody drugs in TNBC has also made some progress. Anti-PD-1 therapy by pembrolizumab can activate T lymphocytes by blocking the interaction between PD-1 and its ligand PD-L1. Studies have shown that pembrolizumab shows some certain clinical benefit, but only in PD-L1-positive TNBC[76]. Another antibody-drug conjugate, sacituzumab govitecan[77,78], which targets the cell surface glycoprotein TROP-2 expressed in more than 90% of TNBC, showed clinical benefit but caused significant adverse reactions, leading to the discontinuation of some TNBC clinical trials. Therefore, it is imperative to explore innovative therapeutic strategies and identify potential drug candidates for TNBC from novel perspectives.

Alterations in the metabolic characteristics of tumors arise from the cumulative effects of genetic mutations and dysregulation of signaling pathways, serving as critical indicators of malignant progression. By considering the metabolic characteristics, re-evaluating TNBC from a holistic perspective may allow us to overcome the limitations of focusing solely on specific targets or signaling pathways[8]. Recently, inhibition of the Warburg effect is emerging as a reliable and promising therapeutic strategy for TNBC. Many compounds that inhibit the Warburg effect have been reported in the treatment of various types of cancer, most of which are inhibitors of key glycolytic enzymes, as well as some small molecules that indirectly affect glycolysis. For instance, the LDHA inhibitor PSTMB was reported to inhibit glycolysis in breast cancer through LDHA suppression, although its anti-tumor activity was suboptimal (MCF-7 cells: $IC_{50} = 84.3 \pm 1.92$ μmol/L)[79]. Moreover, oleanolic acid, a natural product, was found to inhibit aerobic glycolysis at 50 or 100 μg/mL in breast cancer, which also shows limited application prospect due to its low potency[80]. GAPDH inhibitor DC-5163 has been shown to inhibit GAPDH activity to attenuate glycolysis in MDA-MB-231 cells, but its activity was also unsatisfactory (MDA-MB-231 cells: 48 h $IC_{50} = 99.22$ μmol/L, 72 h $IC_{50} = 52.09$ μmol/L)[81]. Therefore, the development of novel inhibitors of Warburg effect with novel mechanisms has significant clinical value for the treatment of TNBC.

In this study, we endeavored to identify novel glycolysis inhibitors from a unique perspective. Given the remarkable contributions of natural products to cancer therapy, exemplified by chemotherapeutic agents such as paclitaxel and colchicine, we aimed to identify novel natural compounds with glycolysis inhibitory activity. We first identified the reported active compounds with a glycolysis inhibitory activity through data mining and literature collection, processed these compounds through machine learning and manual screening, and predicted and evaluated the possible pharmacophore. A natural small molecule, (+)-miliusol, with potential glycolysis inhibitory activity was obtained through preferred pharmacophore screening combined with the glucose uptake capacity screening in the glycolytic subtype TNBC BT-549 cell line. Next, we demonstrated that (+)-miliusol markedly suppresses cell proliferation, the Warburg effect, and migration of TNBC cells, thereby offering preliminary evidence of its therapeutic potential *in vitro*.

PAK1 and ATAD2 are currently emerging targets for cancer therapy, and drug development targeting PAK1 and ATAD2 is also in full swing[35,36]. It is worth noting that both PAK1 and ATAD2 may be involved in the regulation of the Warburg effect, cell proliferation and migration in cancer. In our study, we found that PAK1 and ATAD2 may play an important role in cell death induced by (+)-miliusol. Through bioinformatics analysis of differentially expressed genes, we found that *PAK1* and *ATAD2* were in a relatively central position, and may be involved in regulating (+)-miliusol-induced glycolysis inhibition, cell apoptosis, ER stress and autophagy. After confirming that (+)-miliusol could indeed significantly reduce the expression levels and activities of PAK1 and ATAD2 in TNBC cells, we then knocked down *PAK1* or *ATAD2*, respectively, and found that knockdown of *PAK1* or *ATAD2* alone could barely attenuate the anti-proliferative activity of (+)-miliusol. However, when *PAK1* and *ATAD2* were knocked down simultaneously, the treatment of (+)-miliusol had little effect on cell proliferation, indicating that PAK1 and ATAD2 are both very important for the anti-proliferative effect of (+)-miliusol. Ras−Raf−MEK1/2−ERK1/2 signaling and AKT−mTOR pathway are two known oncogenic signaling pathways which can be activated by PAK1 and ATAD2. We further verified that treatment of (+)-miliusol blocked these two pathways. In addition, (+)-miliusol activated the ULK1 complex, a key component of autophagy initiation, by inhibiting mTOR, which is consistent with significant enrichment in autophagy pathway suggested by transcriptomics analysis.

The role of autophagy in TNBC has also received much attention in recent years[82]. As a mature system of cellular self-recycling, autophagy often plays a dual role in cancer progression. One study found that TNBC had lower levels of basal autophagy, and that dysregulation of autophagy blunted the ability of T cells to kill tumors[83]. Another study found that autophagy also impedes the occurrence of TNBC by inhibiting the stemness of tumor cells[84]. However, autophagy has also been reported to promote drug resistance to the anticancer drug epirubicin in the treatment of TNBC[85]. Therefore, some small molecules that regulate autophagy, including both autophagy activators and inhibitors, have also shown promises in the treatment of TNBC. For instance, the SIRT3 activator ADTL-SA1215 was identified to induce autophagy and exhibit therapeutic potential in TNBC both *in vitro* and *in vivo*[25]. The natural product Ferulic C has also been found to facilitate autophagy-related cell death in TNBC[24]. The autophagy inhibitor hydroxychloroquine (HCQ) has been shown to potentiate the anti-tumor activity of the topoisomerase I inhibitor SN38 in TNBC[86]. Thus, we next investigated the role of (+)-miliusol-induced autophagy in cell proliferation, glycolysis and migration. Unexpectedly, our findings indicate that (+)-miliusol-induced autophagy may counteract the inhibitory effects of (+)-miliusol on glycolysis, cell proliferation, and metastasis. In other words, the induction of autophagy by (+)-miliusol appears to be detrimental to its anti-tumor efficacy.

Translation of mRNA in cancer cells has distinct characteristics compared to that in normal cells. The adaptive mechanism of mRNA translation regulation in cancer enables the tumor to dynamically adapt to various stimuli and cope with survival pressure[87]. EIF3 is the largest and most complex mammalian translation initiation factor, in which EIF3D is involved in regulating the onset and development of tumor metabolic stress by regulating the translation of specific mRNAs, such as c-Jun[12]. By MS-CETSA analysis, we identified EIF3D as a potential direct target of (+)-miliusol, and then applied WB-CETSA experiment, boitin-(+)-miliusol probe, the PROTAC-(+)-miliusol probe for joint confirmation. Molecular docking analysis suggests that (+)-miliusol may interfere with EIF3D-mediated mRNA translation by disrupting the interactions between EIF3D and RPS16 as well as RPS5. The disruption of EIF3D−RPS16−RPS5 complex by (+)-miliusol was then confirmed by protein co-immunoprecipitation. Interestingly, in a separate study, we synthesized a series of derivatives through structural modifications of (+)-miliusol. Among these, derivative ZMF-24 exhibited superior anti-TNBC potential, which may be attributed to its inhibition of EIF3D[88]. However, further validation is required to confirm its target specificity and mechanism of action. Through proteomics, we further found and identified that (+)-miliusol could inhibit the glycolysis and proliferation of TNBC cells by inhibiting the EIF3D−ALKBH5−GLUT4 pathway. (+)-Miliusol can also inhibit the EIF3D−RUVBL1−β-catenin pathway to block the metastasis of TNBC cells. (+)-Miliusol can induce a robust ER stress response in TNBC cells by inhibiting EIF3D−HSP90, which subsequently activates JNK and triggers calcium release, ultimately promoting Caspase-12-mediated apoptosis. Similarly, autophagy induced by (+)-miliusol was not conducive to (+)-miliusol-induced apoptosis. Notably, we evaluated the relative expression levels of EIF3D in a panel of tumor cell lines and normal cells (as shown in Supporting Information Fig. S25) using Western blot analysis, combined with quantitative densitometry and statistical assessment. The results indicated that cells with higher EIF3D expression exhibited greater sensitivity to (+)-miliusol, a finding that aligns well with the compound's demonstrated antitumor efficacy (Fig. S2). This finding suggests that (+)-miliusol holds broad application prospects and may potentially be developed for the treatment of various tumors characterized by high EIF3D expression.

Considering the negative effect of autophagy on TNBC cell death induced by (+)-miliusol, we included an autophagy inhibitor-treated group (CQ, 20 mg/kg) in the nude mouse xenograft experiment. However, the results showed that CQ had no significant effect on the tumor growth in the (+)-miliusol-treated group, with differential effects on the expression of some marker proteins for glycolysis, apoptosis, autophagy, migration and ER stress. Nevertheless, the overall effect on tumor phenotype was minimal. This suggests that the complex role of autophagy in (+)-miliusol-induced cell death remains to be further elucidated, especially in the case of drug treatment with longer duration. It is encouraging to observe that the combination of CQ and (+)-miliusol enhanced the survival rate of tumor-bearing mice treated with (+)-miliusol, thereby providing further evidence for the potential benefits of autophagy inhibition in the future treatment of TNBC using (+)-miliusol. Upon observing that treatment with (+)-miliusol results in weight loss in mice, we conducted comprehensive safety evaluations through blood routine tests, organ HE staining, and analysis of T cell and B cell ratios. These assessments indicate that (+)-miliusol is generally well-tolerated. In addition, T cells exhibited no significant activation in either the blood or tumor tissue, suggesting that (+)-miliusol does not mediate its anti-TNBC effects *via* T cell activation. However, it was noted that the mice experienced diarrhea during the experiment, which may have contributed to the observed weight loss. Further investigation into the underlying mechanisms will be pursued.

5. Conclusions

In conclusion, this study demonstrates that (+)-miliusol acts as a novel inhibitor of the Warburg effect and exhibits therapeutic potential against TNBC both *in vitro* and *in vivo* by targeting EIF3D. Mechanistically, (+)-miliusol suppresses the EIF3D−ALKBH5−GLUT4, EIF3D−HIF1α, and EIF3D−RUVBL1−β-catenin signaling pathways, leading to the inhibition of PAK1, ATAD2, and Snail. These effects consequently attenuate glycolysis and migration in TNBC models. Furthermore, inhibition of EIF3D by (+)-miliusol disrupts protein translation, resulting in endoplasmic reticulum stress and activation of apoptosis mediated by caspase-12 and JNK. Taken together, these results establish a robust mechanistic foundation for targeting EIF3D as a promising therapeutic strategy for TNBC, through impediment of the synthesis of proteins critical for tumor survival.

Acknowledgements

This work was supported in part by National Natural Science Foundation of China (Grants 82173666, 82104060, 82172649, 82373193 and 32070748); Shenzhen Science and Technology Program Grants JCYJ20240813142819026, JCYJ2025060 4144930041; Guangdong Basic and Applied Basic Research Foundation (2024A1515012317); Excellent Scientific and Technological Innovation Training Program of Shenzhen (RCYX20210706092040048); Natural Science Foundation of Top Talent of SZTU Grant (GDRC202125).

Author contributions

Dahong Yao, Zhendan He, and Yue Hao conceived and designed the project; Jin Zhang, Xiya Chen, Lin Jia and Ling Zou performed the cell experiments; Xiaohan Sun and Xiya Chen performed the animal experiments; Dahong Yao carried out the design and synthesis of the compounds; Yan Wu carried out the extraction and separation experiments; Xiaoling Cheng and Le Zhou did the data analysis; Jingnan Huang, Hongchao Zhao and Lingyun Dai carried out MS-CETSA experiment and corresponding data analysis; Jin Zhang, Lin Jia, and Dahong Yao wrote the paper. Dahong Yao, Bo Liu, and Yue Hao checked the manuscript. All authors discussed the results and commented on the manuscript.

Conflicts of interest

All authors declare no potential conflicts of interest.

Appendix A. Supporting information

Supporting information to this article can be found online at https://doi.org/10.1016/j.apsb.2026.03.021.

References

1. Harbeck N, Penault-Llorca F, Cortes J, Gnant M, Houssami N, Poortmans P, et al. Breast cancer. *Nat Rev Dis Primers* 2019;**5**:66.
2. Bianchini G, Balko JM, Mayer IA, Sanders ME, Gianni L. Triple-negative breast cancer: challenges and opportunities of a heterogeneous disease. *Nat Rev Clin Oncol* 2016;**13**:674−90.
3. Garrido-Castro AC, Lin NU, Polyak K. Insights into molecular classifications of triple-negative breast cancer: improving patient selection for treatment. *Cancer Discov* 2019;**9**:176−98.
4. Bianchini G, De Angelis C, Licata L, Gianni L. Treatment landscape of triple-negative breast cancer—expanded options, evolving needs. *Nat Rev Clin Oncol* 2022;**19**:91−113.
5. Pascual J, Turner NC. Targeting the PI3-kinase pathway in triple-negative breast cancer. *Ann Oncol* 2019;**30**:1051−60.
6. Jia H, Truica CI, Wang B, Wang Y, Ren X, Harvey HA, et al. Immunotherapy for triple-negative breast cancer: existing challenges and exciting prospects. *Drug Resist Updates* 2017;**32**:1−15.
7. Leidner R, Sanjuan Silva N, Huang H, Sprott D, Zheng C, Shih YP, et al. Neoantigen T-cell receptor gene therapy in pancreatic cancer. *N Engl J Med* 2022;**386**:2112−9.
8. Gong Y, Ji P, Yang YS, Xie S, Yu TJ, Xiao Y, et al. Metabolic-pathway-based subtyping of triple-negative breast cancer reveals potential therapeutic targets. *Cell Metab* 2021;**33**:51−64.e9.
9. Vander Heiden MG, Cantley LC, Thompson CB. Understanding the Warburg effect: the metabolic requirements of cell proliferation. *Science* 2009;**324**:1029−33.
10. Yang X, Wang Y, Zhao J, Rong H, Chen Y, Xiong M, et al. Coordinated regulation of BACH1 and mitochondrial metabolism through tumor-targeted self-assembled nanoparticles for effective triple negative breast cancer combination therapy. *Acta Pharm Sin B* 2022;**12**:3934−51.
11. Guo R, Deng M, He X, Li M, Li J, He P, et al. Fucoidan-functionalized activated platelet-hitchhiking micelles simultaneously track tumor cells and remodel the immunosuppressive microenvironment for efficient metastatic cancer treatment. *Acta Pharm Sin B* 2022;**12**:467−82.
12. Ma S, Liu JY, Zhang JT. eIF3d: a driver of noncanonical cap-dependent translation of specific mRNAs and a trigger of biological/pathological processes. *J Biol Chem* 2023;**299**:104658.
13. Alard A, Katsara O, Rios-Fuller T, Parra C de la, Ozerdem U, Ernlund A, et al. Breast cancer cell mesenchymal transition and metastasis directed by DAP5/eIF3d-mediated selective mRNA translation. *Cell Rep* 2023;**42**:112646.
14. Zhang F, Xiang S, Cao Y, Li M, Ma Q, Liang H, et al. Correction: EIF3D promotes gallbladder cancer development by stabilizing GRK2 kinase and activating PI3K−AKT signaling pathway. *Cell Death Dis* 2021;**13**:19.
15. Liu Q, Liu J, Zheng D, Zhang R, Xiang Y, Xu F, et al. EIF3D promoted cervical carcinoma through Warburg effect by interacting with GRP78. *J Obstet Gynaecol* 2023;**43**:2130200.
16. Huong DT, Kamperdick C, Sung TV. Homogentisic acid derivatives from *Miliusa balansae*. *J Nat Prod* 2004;**67**:445−7.
17. Xu XY, Tsang SW, Guan YF, Liu KL, Pan WH, Lam CS, et al. *In vitro* and *in vivo* antitumor effects of plant-derived Miliusanes and their induction of cellular senescence. *J Med Chem* 2019;**62**:1541−61.
18. Datta S, Li J, Mahdi F, Jekabsons MB, Nagle DG, Zhou YD. Glycolysis inhibitor screening identifies the bis-geranylacylphloroglucinol protonophore moronone from *Moronobea coccinea*. *J Nat Prod* 2012;**75**:2216−22.
19. Mishra RK, Wei C, Hresko RC, Bajpai R, Heitmeier M, Matulis SM, et al. *In silico* modeling-based identification of glucose transporter 4 (GLUT4)-selective inhibitors for cancer therapy. *J Biol Chem* 2015;**290**:14441−53.
20. Landis CJ, Zhang S, Benavides GA, Scott SE, Li Y, Redmann M, et al. Identification of compounds that decrease glioblastoma growth and glucose uptake *in vitro*. *ACS Chem Biol* 2018;**13**:2048−57.
21. Brito Querido J, Sokabe M, Kraatz S, Gordiyenko Y, Skehel JM, Fraser CS, et al. Structure of a human 48S translational initiation complex. *Science* 2020;**369**:1220−7.
22. Dai L, Prabhu N, Yu LY, Bacanu S, Ramos AD, Nordlund P. Horizontal cell biology: monitoring global changes of protein interaction states with the proteome-wide cellular thermal shift assay (CETSA). *Annu Rev Biochem* 2019;**88**:383−408.
23. Dai L, Zhao T, Bisteau X, Sun W, Prabhu N, Lim YT, et al. Modulation of protein-interaction states through the cell cycle. *Cell* 2018;**173**:1481-94.e13.
24. Yao D, Pan D, Zhen Y, Huang J, Wang J, Zhang J, et al. Ferulin C triggers potent PAK1 and p21-mediated anti-tumor effects in breast cancer by inhibiting Tubulin polymerization *in vitro* and *in vivo*. *Pharmacol Res* 2020;**152**:104605.
25. Zhang J, Zou L, Shi D, Liu J, Zhang J, Zhao R, et al. Structure-guided design of a small-molecule activator of sirtuin-3 that modulates autophagy in triple negative breast cancer. *J Med Chem* 2021;**64**:14192−216.
26. Yao D, Li C, Jiang J, Huang J, Wang J, He Z, et al. Design, synthesis and biological evaluation of novel HDAC inhibitors with improved pharmacokinetic profile in breast cancer. *Eur J Med Chem* 2020;**205**:112648.
27. Daina A, Michielin O, Zoete V. SwissTargetPrediction: updated data and new features for efficient prediction of protein targets of small molecules. *Nucleic Acids Res* 2019;**47**:W357−64.
28. Sherman BT, Hao M, Qiu J, Jiao X, Baseler MW, Lane HC, et al. DAVID: a web server for functional enrichment analysis and functional annotation of gene lists (2021 update). *Nucleic Acids Res* 2022;**50**:W216−21.
29. Liberti MV, Locasale JW. The Warburg effect: how does it benefit cancer cells?. *Trends Biochem Sci* 2016;**41**:211−8.
30. Stine ZE, Schug ZT, Salvino JM, Dang CV. Targeting cancer metabolism in the era of precision oncology. *Nat Rev Drug Discov* 2022;**21**:141−62.
31. Li W, Tanikawa T, Kryczek I, Xia H, Li G, Wu K, et al. Aerobic glycolysis controls myeloid-derived suppressor cells and tumor immunity *via* a specific CEBPB isoform in triple-negative breast cancer. *Cell Metab* 2018;**28**:87−103.e6.
32. Diwanji N, Bergmann A. Basement membrane damage by ROS- and JNK-mediated Mmp2 activation drives macrophage recruitment to overgrown tissue. *Nat Commun* 2020;**11**:3631.
33. Padmanaban V, Krol I, Suhail Y, Szczerba BM, Aceto N, Bader JS, et al. E-cadherin is required for metastasis in multiple models of breast cancer. *Nature* 2019;**573**:439−44.
34. Marrache S, Dhar S. The energy blocker inside the power house: Mitochondria targeted delivery of 3-bromopyruvate. *Chem Sci* 2015;**6**:1832−45.
35. Yao D, Li C, Rajoka MSR, He Z, Huang J, Wang J, et al. P21-activated kinase 1: emerging biological functions and potential therapeutic targets in cancer. *Theranostics* 2020;**10**:9741−66.
36. Fu J, Zhang J, Chen X, Liu Z, Yang X, He Z, et al. ATPase family AAA domain-containing protein 2 (ATAD2): from an epigenetic modulator to cancer therapeutic target. *Theranostics* 2023;**13**:787−809.
37. Cliff TS, Wu T, Boward BR, Yin A, Yin H, Glushka JN, et al. MYC controls human pluripotent stem cell fate decisions through regulation of metabolic flux. *Cell Stem Cell* 2017;**21**:502-16.e9.
38. De Rosa V, Iommelli F, Monti M, Fonti R, Votta G, Stoppelli MP, et al. Reversal of Warburg effect and reactivation of oxidative phosphorylation by differential inhibition of EGFR signaling pathways in non-small cell lung cancer. *Clin Cancer Res* 2015;**21**:5110−20.
39. Xu K, Yin N, Peng M, Stamatiades EG, Shyu A, Li P, et al. Glycolysis fuels phosphoinositide 3-kinase signaling to bolster T cell immunity. *Science* 2021;**371**:405−10.
40. King AJ, Sun H, Diaz B, Barnard D, Miao W, Bagrodia S, et al. The protein kinase Pak3 positively regulates Raf-1 activity through phosphorylation of serine 338. *Nature* 1998;**396**:180−3.

41. Wang Z, Fu M, Wang L, Liu J, Li Y, Brakebusch C, et al. p21-activated kinase 1 (PAK1) can promote ERK activation in a kinase-independent manner. *J Biol Chem* 2013;**288**:20093−9.
42. Coles LC, Shaw PE. PAK1 primes MEK1 for phosphorylation by Raf-1 kinase during cross-cascade activation of the ERK pathway. *Oncogene* 2002;**21**:2236−44.
43. Liu GY, Sabatini DM. mTOR at the nexus of nutrition, growth, ageing and disease. *Nat Rev Mol Cell Biol* 2020;**21**:183−203.
44. Doménech E, Maestre C, Esteban-Martínez L, Partida D, Pascual R, Fernández-Miranda G, et al. AMPK and PFKFB3 mediate glycolysis and survival in response to mitophagy during mitotic arrest. *Nat Cell Biol* 2015;**17**:1304−16.
45. Humpton TJ, Alagesan B, DeNicola GM, Lu D, Yordanov GN, Leonhardt CS, et al. Oncogenic KRAS induces NIX-mediated mitophagy to promote pancreatic cancer. *Cancer Discov* 2019;**9**: 1268−87.
46. Zhang S, Xie Y, Yan F, Zhang Y, Yang Z, Chen Z, et al. Negative pressure wound therapy improves bone regeneration by promoting osteogenic differentiation *via* the AMPK−ULK1−autophagy axis. *Autophagy* 2022;**18**:2229−45.
47. Amaravadi RK, Kimmelman AC, Debnath J. Targeting autophagy in cancer: recent advances and future directions. *Cancer Discov* 2019;**9**: 1167−81.
48. Levy JMM, Towers CG, Thorburn A. Targeting autophagy in cancer. *Nat Rev Cancer* 2017;**17**:528−42.
49. Dai L, Li Z, Chen D, Jia L, Guo J, Zhao T, et al. Target identification and validation of natural products with label-free methodology: a critical review from 2005 to 2020. *Pharmacol Ther* 2020;**216**:107690.
50. Kabir M, Yu X, Kaniskan HÜ, Jin J. Chemically induced degradation of epigenetic targets. *Chem Soc Rev* 2023;**52**:4313−42.
51. Meissner F, Geddes-McAlister J, Mann M, Bantscheff M. The emerging role of mass spectrometry-based proteomics in drug discovery. *Nat Rev Drug Discov* 2022;**21**:637−54.
52. Mukhopadhyay S, Amodeo ME, Lee ASY. eIF3d controls the persistent integrated stress response. *Mol Cell* 2023;**83**:3303-13.e6.
53. Lee AS, Kranzusch PJ, Doudna JA, Cate JHD. eIF3d is an mRNA cap-binding protein that is required for specialized translation initiation. *Nature* 2016;**536**:96−9.
54. Jha S, Dutta A. RVB1/RVB2: running rings around molecular biology. *Mol Cell* 2009;**34**:521−33.
55. Tang C, Ke M, Yu X, Sun S, Luo X, Liu X, et al. GART functions as a novel methyltransferase in the RUVBL1/*β*-Catenin signaling pathway to promote tumor stemness in colorectal cancer. *Adv Sci (Weinh)* 2023; **10**:e2301264.
56. Li C, Lu K, Yang C, Du W, Liang Z. EIF3D promotes resistance to 5-fluorouracil in colorectal cancer through upregulating RUVBL1. *J Clin Lab Anal* 2023;**37**:e24825.
57. Qu J, Yan H, Hou Y, Cao W, Liu Y, Zhang E, et al. RNA demethylase ALKBH5 in cancer: from mechanisms to therapeutic potential. *J Hematol Oncol* 2022;**15**:8.
58. Liu X, Li P, Huang Y, Li H, Liu X, Du Y, et al. M^6A demethylase ALKBH5 regulates FOXO1 mRNA stability and chemoresistance in triple-negative breast cancer. *Redox Biol* 2024;**69**:102993.
59. Liu H, Lyu H, Jiang G, Chen D, Ruan S, Liu S, et al. ALKBH5-mediated m^6A demethylation of GLUT4 mRNA promotes glycolysis and resistance to HER2-targeted therapy in breast cancer. *Cancer Res* 2022;**82**:3974−86.
60. Tamada M, Suematsu M, Saya H. Pyruvate kinase M2: multiple faces for conferring benefits on cancer cells. *Clin Cancer Res* 2012;**18**: 5554−61.
61. Zhu S, Guo Y, Zhang X, Liu H, Yin M, Chen X, et al. Pyruvate kinase M2 (PKM2) in cancer and cancer therapeutics. *Cancer Lett* 2021;**503**:240−8.
62. Yang W, Xia Y, Hawke D, Li X, Liang J, Xing D, et al. PKM2 phosphorylates histone H3 and promotes gene transcription and tumorigenesis. *Cell* 2014;**158**:1210.
63. Marciniak SJ, Chambers JE, Ron D. Pharmacological targeting of endoplasmic reticulum stress in disease. *Nat Rev Drug Discov* 2022; **21**:115−40.
64. Chen X, Cubillos-Ruiz JR. Endoplasmic reticulum stress signals in the tumour and its microenvironment. *Nat Rev Cancer* 2021;**21**:71−88.
65. Thompson L, Depledge DP, Burgess HM, Mohr I. An eIF3d-dependent switch regulates HCMV replication by remodeling the infected cell translation landscape to mimic chronic ER stress. *Cell Rep* 2022;**39**:110767.
66. Zhou Y, Lee J, Reno CM, Sun C, Park SW, Chung J, et al. Regulation of glucose homeostasis through a XBP-1−FoxO1 interaction. *Nat Med* 2011;**17**:356−65.
67. Ota A, Wang Y. Cdc37/Hsp90 protein-mediated regulation of IRE1α protein activity in endoplasmic reticulum stress response and insulin synthesis in INS-1 cells. *J Biol Chem* 2012;**287**:6266−74.
68. Cerchietti LC, Lopes EC, Yang SN, Hatzi K, Bunting KL, Tsikitas LA, et al. A purine scaffold Hsp90 inhibitor destabilizes BCL-6 and has specific antitumor activity in BCL-6-dependent B cell lymphomas. *Nat Med* 2009;**15**:1369−76.
69. Stefan CJ. Endoplasmic reticulum-plasma membrane contacts: principals of phosphoinositide and calcium signaling. *Curr Opin Cell Biol* 2020;**63**:125−34.
70. Killock D. AKT inhibition improves OS in TNBC. *Nat Rev Clin Oncol* 2020;**17**:135.
71. Pantelidou C, Sonzogni O, De Oliveria Taveira M, Mehta AK, Kothari A, Wang D, et al. PARP inhibitor efficacy depends on $CD8^+$ T-cell recruitment *via* intratumoral STING pathway activation in BRCA-deficient models of triple-negative breast cancer. *Cancer Discov* 2019;**9**:722−37.
72. Ibrahim YH, García-García C, Serra V, He L, Torres-Lockhart K, Prat A, et al. PI3K inhibition impairs BRCA1/2 expression and sensitizes BRCA-proficient triple-negative breast cancer to PARP inhibition. *Cancer Discov* 2012;**2**:1036−47.
73. Turner NC, Telli ML, Rugo HS, Mailliez A, Ettl J, Grischke EM, et al. A phase II study of talazoparib after platinum or cytotoxic non-platinum regimens in patients with advanced breast cancer and germline BRCA1/2 mutations (ABRAZO). *Clin Cancer Res* 2019;**25**: 2717−24.
74. Schmid P, Abraham J, Chan S, Wheatley D, Brunt AM, Nemsadze G, et al. Capivasertib plus paclitaxel *versus* placebo plus paclitaxel as first-line therapy for metastatic triple-negative breast cancer: the PAKT trial. *J Clin Oncol* 2020;**38**:423−33.
75. Shi Z, Wulfkuhle J, Nowicka M, Gallagher RI, Saura C, Nuciforo PG, et al. Functional mapping of AKT signaling and biomarkers of response from the FAIRLANE trial of neoadjuvant ipatasertib plus paclitaxel for triple-negative breast cancer. *Clin Cancer Res* 2022;**28**:993−1003.
76. Killock D. Pembrolizumab can delay progression of TNBC. *Nat Rev Clin Oncol* 2021;**18**:64.
77. Bardia A, Mayer IA, Diamond JR, Moroose RL, Isakoff SJ, Starodub AN, et al. Efficacy and safety of anti-Trop-2 antibody drug conjugate sacituzumab govitecan (IMMU-132) in heavily pretreated patients with metastatic triple-negative breast cancer. *J Clin Oncol* 2017;**35**:2141−8.
78. Cardillo TM, Sharkey RM, Rossi DL, Arrojo R, Mostafa AA, Goldenberg DM. Synthetic lethality exploitation by an Anti-Trop-2-SN-38 antibody−drug conjugate, IMMU-132, plus PARP inhibitors in BRCA1/2-wild-type triple-negative breast cancer. *Clin Cancer Res* 2017;**23**:3405−15.
79. Kim EY, Chung T-W, Han CW, Park SY, Park KH, Jang SB, et al. A novel lactate dehydrogenase inhibitor, 1-(phenylseleno)-4-(trifluoromethyl) benzene, suppresses tumor growth through apoptotic cell death. *Sci Rep* 2019;**9**:3969.
80. Liu J, Wu N, Ma L, Liu M, Liu G, Zhang Y, et al. Oleanolic acid suppresses aerobic glycolysis in cancer cells by switching pyruvate kinase type M isoforms. *PLoS One* 2014;**9**:e91606.

81. Li T, Tan X, Yang R, Miao Y, Zhang M, Xi Y, et al. Discovery of novel glyceraldehyde-3-phosphate dehydrogenase inhibitor *via* docking-based virtual screening. *Bioorg Chem* 2020;**96**:103620.
82. Abd El-Aziz YS, Gillson J, Jansson PJ, Sahni S. Autophagy: a promising target for triple negative breast cancers. *Pharmacol Res* 2022;**175**:106006.
83. Li ZL, Zhang HL, Huang Y, Huang JH, Sun P, Zhou NN, et al. Autophagy deficiency promotes triple-negative breast cancer resistance to T cell-mediated cytotoxicity by blocking tenascin-C degradation. *Nat Commun* 2020;**11**:3806.
84. Park JW, Kim Y, Lee SB, Oh CW, Lee EJ, Ko JY, et al. Autophagy inhibits cancer stemness in triple-negative breast cancer *via* miR-181a-mediated regulation of ATG5 and/or ATG2B. *Mol Oncol* 2022;**16**: 1857−75.
85. Chittaranjan S, Bortnik S, Dragowska WH, Xu J, Abeysundara N, Leung A, et al. Autophagy inhibition augments the anticancer effects of epirubicin treatment in anthracycline-sensitive and -resistant triple-negative breast cancer. *Clin Cancer Res* 2014;**20**:3159−73.
86. Wang H, Bai H, Wang J, Zhou X, Chen H, Wang L, et al. Nanoprodrug ratiometrically integrating autophagy inhibitor and genotoxic agent for treatment of triple-negative breast cancer. *Biomaterials* 2022;**283**: 121458.
87. Fabbri L, Chakraborty A, Robert C, Vagner S. The plasticity of mRNA translation during cancer progression and therapy resistance. *Nat Rev Cancer* 2021;**21**:558−77.
88. Zhao X, Cheng X, Liu Z, Chen W, Hao W, Ma S, et al. Design, synthesis and biological evaluation of plant-derived miliusol derivatives achieve TNBC profound regression *in vivo*. *Eur J Med Chem* 2024;**279**:116882.